



Earliest Ediacaran speleothems and their implications for terrestrial life after the Marinoan snowball Earth

Tian Gan^{a,b,c,d,h}, Guanghong Zhou^{e,f,*}, Taiyi Luo^{a,*}, Ke Pang^{c,d}, Mingzhong Zhou^g, Weijun Luo^h, Shijie Wang^h, Shuhai Xiao^{b,*}

^a State Key Laboratory of Ore Deposit Geochemistry, Institute of Geochemistry, Chinese Academy of Sciences, Guiyang 550081, China

^b Department of Geosciences, Virginia Tech, Blacksburg, VA 24061, USA

^c State Key Laboratory of Palaeobiology and Stratigraphy, Nanjing Institute of Geology and Palaeontology, Chinese Academy of Sciences, Nanjing 210008, China

^d University of Chinese Academy of Sciences, Beijing 101408, China

^e School of Geography and Resources, Guizhou Education University, Guiyang 550018, China

^f Guizhou Provincial Key Laboratory of Geographic State Monitoring of Watershed, Guizhou Education University, Guiyang 550018, China

^g School of Geographical and Environmental Sciences, Guizhou Normal University, Guiyang 550001, China

^h State Key Laboratory of Environmental Geochemistry, Institute of Geochemistry, Chinese Academy of Sciences, Guiyang 550081, China

ARTICLE INFO

Keywords:

South China

Ediacaran

Doushantuo Formation

Cap dolostone

Karstification

Terrestrial microbial ecosystem

ABSTRACT

Cryogenian snowball Earth glaciations may have had disastrous impacts on the biosphere, particularly the terrestrial ecosystem. However, how the terrestrial ecosystem responded to and recovered from these glaciations remains poorly understood. Speleothems offer important insights into terrestrial life because their formation is critically dependent on soil CO₂ derived from microbial respiration. Here we report the wide distribution of miniature paleo-speleothems from the ~ 635 Ma Doushantuo cap dolostone in South China and assess their implications for the recovery of terrestrial life after the terminal Cryogenian Marinoan glaciation. The ~ 3-m-thick cap dolostone was deposited during the initial transgression following deglaciation but subsequently experienced subaerial exposure due to post-glacial rebound, which resulted in the development of extensive sheet-cavities in the cap dolostone and a widespread karstic surface atop the cap dolostone. The sheet-cavities were filled with multiple generations of minerals, including isopachous dolomite interpreted to have formed in the phreatic zone, speleothems consisting of fibrous calcite interpreted to have formed in the vadose zone, as well as later phases (i.e., isopachous radial chalcedony, crystalline quartz, and blocky calcite). The Doushantuo speleothems are millimeter-to-centimeter in size and include gravitational speleothems (stalactites and stalagmites) and non-gravitational speleothems (helictites, moonmilk, botryoids, and flat crusts). Some of them were secondarily silicified by hydrothermal fluids before a renewed transgression in which ~ 632 Ma shales overlying the cap dolostone were deposited. The wide distribution of Doushantuo speleothems and the preservation of microfossils in these speleothems indicate the presence of an active soil-microbial ecosystem in the earliest Ediacaran Period and the rapid recovery of terrestrial life after the Marinoan snowball Earth.

1. Introduction

The Cryogenian Marinoan glaciation (ca. 650–635 Ma) likely had a catastrophic impact on both the marine and terrestrial ecosystems (Hoffman et al., 2017). The rapid post-glacial recovery of the marine ecosystem is evidenced by microbialites (Cloud et al., 1974; Romero et al., 2020) and eukaryotic biomarkers (van Maldegem et al., 2019) in cap dolostones atop Marinoan glacial deposits. The recovery of non-marine ecosystems in terrestrial (e.g., lacustrine, fluvial, intertidal,

and otherwise subaerially exposed) environments, however, has not been investigated, although paleosols (Retallack, 2021; Retallack et al., 2021; Retallack et al., 2015), paleontological data (Wellman and Strother, 2015), biosedimentary structures (Homann et al., 2018; Noffke et al., 2006; Prave, 2002), and geochemical data (Kennedy et al., 2006; Kump, 2014) hint that these environments had been biologically colonized prior to the Cryogenian Period. Possible supraglacial cryoconite ponds could have provided refugia for terrestrial microbes and freshwater oligotrophic ecosystems during the glaciation (Hoffman et al.,

* Corresponding authors.

E-mail addresses: zhouguanghong@gznc.edu.cn (G. Zhou), luotaiyi@mail.gyig.ac.cn (T. Luo), xiao@vt.edu (S. Xiao).

<https://doi.org/10.1016/j.precamres.2022.106685>

Received 5 January 2022; Received in revised form 21 March 2022; Accepted 17 April 2022

Available online 11 May 2022

0301-9268/© 2022 Elsevier B.V. All rights reserved.

2017), but how the terrestrial ecosystems recovered after the glaciation is largely unknown. The recovery of terrestrial ecosystems is particularly important for the flourishing of the entire biosphere because they facilitate the liberation of bio-available nutrients from minerals (van der Heijden et al., 2008) and the supply of these nutrients to the marine realm (Thomazo et al., 2018).

Karstic speleothems are terrestrial deposits that archive remarkable paleoenvironment records (Verheyden et al., 2000). Studies of modern karstic caves suggest that speleothem deposition is mostly controlled by the evolution of CO₂ contents in drip-waters, which originate from meteoric precipitation at equilibrium with atmospheric CO₂ and then become CO₂-supersaturated when interacting with soil-ecosystems where microbial respiration and organic decomposition led to locally high [CO₂], followed by CO₂ degassing in caves (Brasier, 2011; Fairchild et al., 2006; White, 2005). Thus, paleo-speleothems, such as dripstones, micro-stalactites, and stromatolitic coatings (Álvarez and Clausen, 2010; Freydet and Verrecchia, 2002), are important evidence for subaerial exposure, paleo-pedogenesis, and active soil-ecosystems. Not only do karstic speleothems provide indirect evidence for microbial life, but cavities (including karstic cavities) may also have provided habitable niches for early life on Earth (Homann et al., 2016; Rasmussen et al., 2009). Microfossils can be preserved in such cavities, thus providing direct evidence for terrestrial microbes (Gan et al., 2021). However, the Precambrian record of paleo-speleothems is rare. Limited examples include the oldest known speleothems from ~ 1.27 Ga Dismal Lakes Group, Arctic Canada (Glover, 2006), silicified speleothems from > 1.1 Ga Mescal Limestone, central Arizona, U.S.A. (Skotnicki and Knauth, 2007), and dolomite speleothems from the late Ediacaran Dengying Formation (551–539 Ma), South China (Ding et al., 2019).

Paleo-karstic surfaces atop 635 Ma cap dolostones in northwestern Africa (Shields et al., 2007), western United States (Creveling et al., 2016), and South China (Zhou et al., 2010) offer an opportunity to explore paleo-speleothems in order to illuminate terrestrial life and environments after the Cryogenian Marinoan glaciation. Here we document six types of microspeleothems within sheet-cavities in the 635 Ma cap dolostone in South China. These paleo-speleothems confirm a post-glacial isostatic rebound event as documented previously (Zhou et al., 2010). More importantly, together with the microfossils preserved in the sheet-cavities (Gan et al., 2021), these paleo-speleothems support a rapid re-establishment of the terrestrial soil-microbial ecosystem following the termination of the Marinoan snowball Earth event.

2. Geological setting and sampled location

The Ediacaran Doushantuo Formation in South China (635–551 Ma) is well exposed on the Yangtze Block (Fig. 1A–B). The Doushantuo Formation directly overlies the terminal Cryogenian glacial diamictite (Nantuo Formation) and underlies the upper Ediacaran Dengying Formation or Liuchapo Formation (Fig. 1C). The successions of the Doushantuo Formation studied in this research—including the Zhangcunping (ZCP), Xiangerwan (XEW), Xiaofenghe (XFH), Jiulongwan (JLW), Huajipo (HJP), Tianjiayuanzi (TJYZ), Beidoushan (BDS), Datang (DT), Mukong (MK), Daping (DP), Songlin (SL), and Wenghui (WH) sections—represent deposition in the inner shelf, shelf lagoon, outer shelf, and slope facies. The thickness of the Doushantuo Formation varies from ~ 90 m at the inner-shelf Zhangcunping section, to ~ 150 m at the shelf-lagoon Jiulongwan section, to ~ 40 m at the outer-shelf Beidoushan section (Jiang et al., 2011; Jiang et al., 2008; Wang et al., 2016; Xiao et al., 2012; Xiao et al., 2014a; Zhou et al., 2017a). Facies variations of the Doushantuo Formation were described by Jiang et al. (2011) and are summarized below, with a focus on the sections studied in this research.

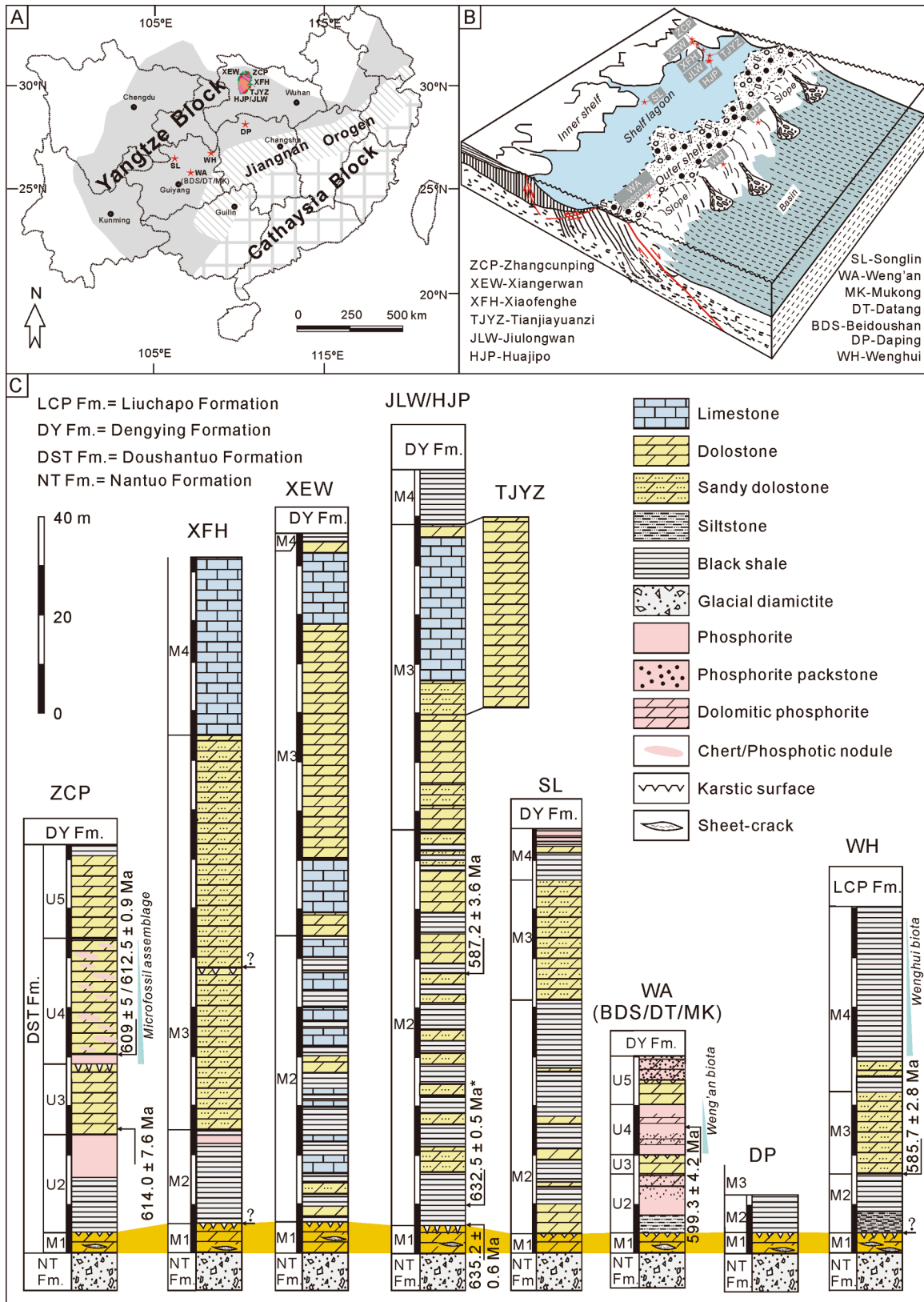
Doushantuo successions in the shelf-lagoon facies are best exemplified around southern Huangling anticline and particularly around the Yangtze Gorges area of Hubei Province, for example at the Xiangerwan (N31°12'56.2", E110°57'57.0") (An et al., 2015; Wei et al., 2019),

Xiaofenghe (N30°48'54", E111°03'20") (Xiao et al., 2012), Jiulongwan (N30°48'54", E111°03'20") (McFadden et al., 2008), Huajipo (N30°46'55.69", E111°2'1.75") (Wei et al., 2019; Xiao et al., 2012), and Tianjiayuanzi section (N30°49'8", E111°4'8") (Lu et al., 2012). Here, the Doushantuo Formation is subdivided into four lithostratigraphic members (Fig. 1C). Member I or M1 (~5 m in thickness) at the basal Doushantuo Formation represents the cap dolostone and is characterized by sheet-cracks and tepee-like structures (Jiang et al., 2006). At some sections (e.g., Xiangerwan), the cap dolostone is capped by a karstic surface with visible topographic reliefs (Fig. 1C, 2A). The depositional age of M1 is constrained by two indistinguishable zircon U–Pb ages—634.57 ± 0.88 Ma immediately below and 635.23 ± 0.57 Ma immediately above the cap dolostone, indicating that the cap dolostone was deposited within one million years around 635 Ma (Zhou et al., 2019). Member II or M2 consists of ~ 80 m of black shale intercalated with muddy/silty dolostone, with local development of thin phosphorite beds (e.g., at Xiaofenghe section, Fig. 1C). In the Yangtze Gorges area, a zircon U–Pb age of 632.5 ± 0.5 Ma has been reported from a horizon in M2 about 5 m above the cap dolostone (Condon et al., 2005), and a Re–Os age of 587.2 ± 3.6 Ma has been reported from black shales in middle M2 (Yang et al., 2021). Member III or M3 is ~ 80 m in thickness and composed of medium- to thick-bedded dolostone, with thin-bedded limestone in the upper M3 at some sections (e.g., Jiulongwan, Huajipo, Xiaofenghe, and Xiangerwan; Fig. 1C). Member IV or M4 is ~ 2–10 m in thickness and consists of black shales. The Miaohu Member in the Yangtze Gorges area, which hosts carbonaceous macroalgal fossils of the Miaohu biota (Xiao et al., 2002) and is capped by a 551.1 ± 0.7 Ma tuffaceous layer (Condon et al., 2005), is variously correlated with upper M4 (Xiao et al., 2017; Zhou et al., 2017a) or regarded as younger than M4 (An et al., 2015).

Other shelf-lagoon sections of the Doushantuo Formation have lithostratigraphic successions similar to those around the Huangling anticline. For example, at the Songlin section (N27°44'3", E106°43'31") in Zunyi, Guizhou Province, the Doushantuo cap dolostone (M1, 4 m in thickness) is characterized by sheet-cracks, stromatolite-like cavities, and tepee-like structures, with a distinct karstic surface at the top (Fig. 1C, 2C). M2 (~47 m in thickness) is mainly composed of micritic dolomite in the lower part and siltstone and black shale in the upper part. M3 (~23 m in thickness) consists of grey dolostone intercalated with thin siltstones and shales. M4 (~16 m in thickness) is featured with black shale and dolomicrite containing chert nodules, phosphorite, and phosphatic shale (Zhang et al., 2020).

Doushantuo successions in upper slope facies—for example, the Daping section (N28°59'01", E110°27'42") in Hunan Province and at the Wenghui section (N27°49'55", E109°01'32") in Guizhou Province—are broadly similar to those in the shelf-lagoon facies, except that black shales are comparatively more dominant in M2. A Re–Os age of 585.7 ± 2.8 Ma has been reported from M2 black shales near Wenghui (Yang et al., 2021). In this study, we logged only the lower Doushantuo Formation at Daping, where the upper Doushantuo is not well exposed, and examined the Wenghui section, which is best known for carbonaceous macroalgal fossils of the Wenghui biota hosted in M4 black shale (Wang et al., 2016; Zhu et al., 2008).

In contrast to shelf-lagoon and upper slope facies, the Doushantuo Formation deposited in shallow-water inner shelf and outer shelf facies—for example, the Zhangcunping section (N31°17'34", E111°12'30") in Hubei Province as well as the Beidoushan (N27°01'40", E107°23'22"), Datang (N27°01'54.5", E107°24'08.4"), and Mukong (N27°05'32", E107°37'43") sections in the Weng'an area of Guizhou Province—are lithostratigraphically different in the presence of multiple economic phosphorite intervals. Thus, the lithostratigraphic divisions of the Doushantuo Formation are described in units to be differentiated from the four members mentioned above. These include five units in Weng'an (Xiao et al., 2014a) and 7–10 units at Zhangcunping (Liu et al., 2009; Ouyang et al., 2019; Wang et al., 2017; Zhou et al., 2017a). For simplicity, the five-unit division scheme in Weng'an is adopted here



(caption on next page)

Fig. 1. Geological and paleogeographic maps showing sample localities and stratigraphic columns of the Ediacaran Doushantuo Formation at the Zhangcunping (ZCP), Xiaofenghe (XFH), Xiangerwan (XEW), Jiulongwan (JLW), Huajipo (HJP), Tianjiayuanzi (TJYZ), Songlin (SL), Weng'an (WA; with three adjacent sections at Beidoushan – BDS, Datang – DT, and Mukong – MK), Daping (DP), and Wenghui (WH) sections, South China. (A) Geological map showing major tectonic units and sample localities. Pink oval marks the Huangling anticline in the northern Yangtze Block. (B) Paleogeographic box diagram showing depositional facies and approximate paleogeographical location of sample localities. (C) Stratigraphic columns of the Doushantuo Formation at the sample localities. ZCP section modified from Ouyang et al. (2019); XEW section from Wei et al. (2019); JLW & HJP sections from Xiao et al. (2012) and Wei et al. (2019); TJYZ section from Lu et al. (2012); XFH section from Xiao et al. (2012); SL section from Zhang et al. (2020); WA section from Xiao et al. (2014a); and WH section from Wang et al. (2016). Question marks indicate that a karstic surface is unclear at sampling locations but can be observed in nearby sections. Radiometric ages: Pb–Pb whole-rock age of 599.3 ± 4.2 Ma from Weng'an (Barfod et al., 2002), SIMS zircon U–Pb age of 609 ± 5 Ma from Zhangcunping (Zhou et al. (2017a) which has been updated as 612.5 ± 0.9 Ma using CA-ID-TIMS (Yang et al., 2021), SHRIMP zircon U–Pb age of 614.0 ± 7.6 Ma from Zhangcunping (Liu et al., 2009), Re–Os age of 587.2 ± 3.6 Ma from a section near Jiulongwan and Huajipo (Yang et al., 2021), Re–Os age of 585.7 ± 2.8 Ma from a section near Wenghui (Yang et al., 2021), and CA-ID-TIMS zircon U–Pb ages of 635.2 ± 0.6 Ma and 632.5 ± 0.5 Ma from sections near Jiulongwan and Huajipo (Condon et al., 2005). (For interpretation of the references to color in this figure legend, the reader is referred to the web version of this article.)

(Fig. 1C). The lowermost unit or U1 is equivalent to M1 described above and represents a 4-meter-thick cap dolostone characterized by abundant sheet-cracks and tepee-like structures, with a distinct karstic surface at the top (Fig. 1C, 2D–E). The second unit or U2 (~10 m in thickness) consists of shales and siltstones followed by phosphorite (the lower phosphorite in the Weng'an area). The third unit or U3 (~2 m in thickness) is composed of light grey and thick-bedded dolostone with another karstic surface on the top. A U–Pb zircon age of 614.0 ± 7.6 Ma has been reported from Zhangcunping in strata equivalent to the basal U3 (Liu et al., 2009). The fourth unit or U4 (~10 m in thickness) consists of phosphorite and dolomitic phosphorite (the upper phosphorite in the Weng'an area). A whole-rock Pb–Pb isochron age of 599.3 ± 4.2 Ma has been reported from the middle U4 in the Weng'an area (Barfod et al., 2002). U4 in the Weng'an area contains the Weng'an biota and yields multicellular algae and putative lichens and metazoans (Xiao et al., 2014a; Yuan et al., 2005). The fifth unit or U5 (~10 m in thickness) is composed of thick-bedded dolostone (~5 m in thickness) and phosphatic dolostone (~5 m in thickness). A U–Pb zircon age of 609 ± 5 Ma has been reported from Zhangcunping in strata equivalent to the basal U5 (Zhou et al., 2017a), although this horizon has been re-dated as 612.5 ± 0.9 Ma and the age has been reinterpreted as a detrital zircon age (Yang et al., 2021). Additional strata—including a thin black shale unit in the topmost Doushantuo Formation that is likely equivalent to M4 in shelf lagoon facies—are present at Zhangcunping (Liu et al., 2009; Ouyang et al., 2019; Zhou et al., 2017a) but absent in the Weng'an area (Xiao et al., 2014a; Xiao et al., 2014b).

Stratigraphic correlation of the Doushantuo Formation between shelf lagoon and inner/outer shelf sections is not entirely resolved. Specifically, the correlation between U2–4 and M2 is suggested by biostratigraphic data but needs to be tested with independent chronostratigraphic data (Liu and Moczydłowska, 2019; Liu et al., 2014; Xiao et al., 2012; Xiao et al., 2014b). Regardless and most relevant to the current study, the correlation between U1 and M1, both representing the basal Ediacaran cap dolostone, is universally adopted. Accepting this correlation, it follows that the cap dolostone in all facies is bracketed by a zircon U–Pb age of 634.6 ± 0.9 Ma from the topmost Nantuo Formation (Zhou et al., 2019) and a zircon U–Pb age of 635.2 ± 0.6 Ma from immediately above the cap dolostone (Fig. 1C) (Condon et al., 2005). An additional minimum age constraint on the cap dolostone and the karstification surface atop the cap dolostone is provided by a zircon U–Pb age of 632.5 ± 0.5 Ma from lower M2 in the Yangtze Gorges area (Fig. 1C) (Condon et al., 2005).

3. Material and methods

Thirty-one sheet-crack samples were collected from the basal Ediacaran cap dolostone of the Doushantuo Formation at eight sections. These samples were subjected to petrographic analysis, including one (ZCP-1) from the Zhangcunping section, three (QBN-003, RVS-1, and TJYZ) from the Tianjiayuanzi section, six (14XFH-1, 14XFH-3, 14XFH-5, 14XFH-7, XFH-4, and XFH/2.5) from the Xiaofenghe section, one (HJP-CL-2.4) from Huajipo section, one (19JLW-12) from Jiulongwan section,

six (19DPc1-1, 19DPc1-2, 19DPc1-3, 19DP2-2z, 19DP2-2D, and 19DP2-2f1) from the Daping section, five from the Wenghui (16WH-1, 16WH-2, 16WH-3, 16WH-4, and 16WH-9) section, and eight (18BDS-2, 18BDS-4, 18BDS-7, 18BDS-9, 18BDS-12, 18WA-6d, 18WA-7b, and WA-3) from the Beidoushan section. Petrographic thin sections of various thicknesses (30 μ m, 100 μ m, and 200 μ m) and polished slabs were cut perpendicular or parallel to the bedding plane and were investigated using transmitted light microscopy (TLM), reflected light microscopy (RLM), epifluorescence light microscopy (ELM), cathodoluminescence (CL) microscopy, backscattered scanning electron microscopy (BSEM), and micro-X-ray fluorescence (μ XRF) scanner.

TLM and RLM images were acquired on a Leica DM4500P microscope coupled with a Nikon D750 digital camera at the Institute of Geochemistry, Chinese Academy of Sciences (IGCAS), a Zeiss AxioScope A1 microscope with an Axiocam 512 digital camera at Virginia Tech, and an Olympus SZ16 microscope with a DP27 digital camera at Virginia Tech. ELM and BSEM observations were carried out at IGCAS. ELM images were acquired on a Zeiss scope A1 with an HBO 100 epifluorescence light source. CL microscopic observation of thin sections was carried out on a Reliotron luminoscope (HC1-LM) equipped with a Nikon polarization microscope (LV100N POL) with a digital camera (DS-Ri1) at the IGCAS. CL images were collected at 5–10 kV acceleration voltage and a beam current of 0.5 mA under 80 to 120 mTorr vacuum. BSEM images were taken on a JEOL JSM-7800F field scanning electron microscope. Micro X-ray fluorescence images were produced using an IXRF Systems ATLAS μ XRF scanner at the Third Institute of Oceanography, Ministry of Natural Resources, China. X-Ray source was operated under maximum energy settings (50 kV) with 11 μ m spacing. The scanning frequency was set to 1.0 (Tc = 1.0) and the dwell time at each point was set to 30 s.

4. Field observations: Karstic surface and sheet-cavities

An uneven surface, interpreted as a karstic surface, atop basal Ediacaran cap dolostones can be observed at multiple stratigraphic sections in South China from inner shelf to outer shelf facies, indicating a sub-aerial exposure event at the regional scale (Zhou et al., 2010). In our survey, it was observed at the Zhangcunping, Xiangerwan, Datang, Mukong, and Songlin sections (Fig. 1C, 2). The top surface of the basal Doushantuo cap dolostone, which is typically 2–5 m thick, has a considerable topographic relief of up to 2–3 m (e.g., the Songlin section, Fig. 2C). At Xiangerwan and Mukong, this surface is coated by 2–3 cm thick barite fans growing upward. At Mukong, a 10–20 cm thick basal conglomerate bed, mainly composed of dolomite clasts and boulders (Fig. 2F), also occurs at this surface. Black shale or thin-bedded dolostone that overlies the cap dolostone exhibits an onlapping relationship with the karstic surface (Fig. 2A, 2D), indicating that the topographic relief predates the deposition of strata above the cap dolostone.

Sheet-cracks/sheet-cavities are most abundant in the lower 1–2 m of the cap dolostone (Jiang et al., 2006). They are commonly parallel to bedding (hence the term sheet-cracks; Fig. 3A–B), even when the sedimentary beds warp to form tepee-like structures (Fig. 3A, 3C). Their size



Fig. 2. Field photographs of subaerially exposed and karstified surface (dashed lines) atop Doushantuo cap dolostone at Xiangerwan (A, Courtesy of Chuanming Zhou), Zhangchunping (B), Songlin (C), Datang (D), and Mukong (E). Labeled box in (E) marks area magnified in (F). (F) shows basal conglomerate above the exposure surface at Mukong (E), composed of dolomite clasts (red arrows), dolomite boulders (white arrows), and quartz clasts (blue arrow). Topographic relief of the karstic surface is up to 2 m. The cap dolostone (marked as “Cap”) is overlain by thin-bedded dolostone at Xiangerwan and Songlin (“M2” in A and C), shaley dolostone at Mukong (“U2” in E), or black shale at Datang (“U2” in D) and Zhangchunping (“U2” in B). Geologist in (A–B, E) about 170 cm in height, and rock hammers (circled in C–D) about 30 cm in length. (For interpretation of the references to color in this figure legend, the reader is referred to the web version of this article.)

ranges from millimeters to decimeters in height and from centimeters to meters in lateral extent (Fig. 3A–D). Some sheet-cracks have sharp corners or terminations (Fig. 3A–B, 3E), indicating a mechanical origin; these cracks may have been physically initiated by an increase in pore-fluid pressure (Corkeron, 2007; Gammon, 2012; Gammon et al., 2012) or a decrease in hydrostatic pressure (Hoffman and Macdonald, 2010). However, most sheet-cracks are expanded cavities (Fig. 3D) with somewhat rounded walls (Fig. 3F), indicating that they were subsequently augmented by chemical dissolution, probably related to subaerial exposure and karstification during post-glacial rebound (Zhou et al., 2010). Indeed, in some cases, the sheet-cracks can be seen to be physically connected with the karstic surface atop the Doushantuo cap dolostone (Zhou et al., 2010). Thus, considering the important roles of both physical and chemical processes, the sheet-cracks are hereafter referred to as sheet-cavities.

5. Petrographic observations of multiple generations of cements in sheet-cavities

Previous authors have identified multiple generations of cements in

the sheet-cavities (Zhou et al., 2010; Zhou et al., 2017b). Typically, these cements begin with isopachous dolomite ± barite ± pyrite, followed by isopachous fibrous calcite, siliceous phases (including isopachous radial chalcedony and crystalline quartz) ± pyrite, and blocky calcite/dolomite ± barite ± pyrite ± sphalerite. Observations described below indicate that the cements grew centripetally toward the center of the sheet-cavities.

Outcrop and hand-specimen observations in this study largely confirm the sequence of cements described above. Based on cement stratigraphy, the earliest generation of cement is light-colored isopachous dolomite that constitutes a thin layer of cement on the walls of sheet-cavities against the cap dolostone matrix (Fig. 3D–E). The isopachous dolomite is overlain by chalcedony, crystalline quartz, and light- to dark-grey blocky calcite/dolomite (Fig. 3D–F). The occurrence of these cements is variable and depends on the dimension of sheet-cavities and the paleogeographical setting. Smaller sheet-cavities are typically filled with isopachous dolomite only, whereas larger ones can be filled with two or more generations of cements (Fig. 3E–F). In upper slope facies (e.g., Daping section), a complete succession of cements can be observed in large sheet-cavities (Fig. 3E), whereas in outer shelf facies

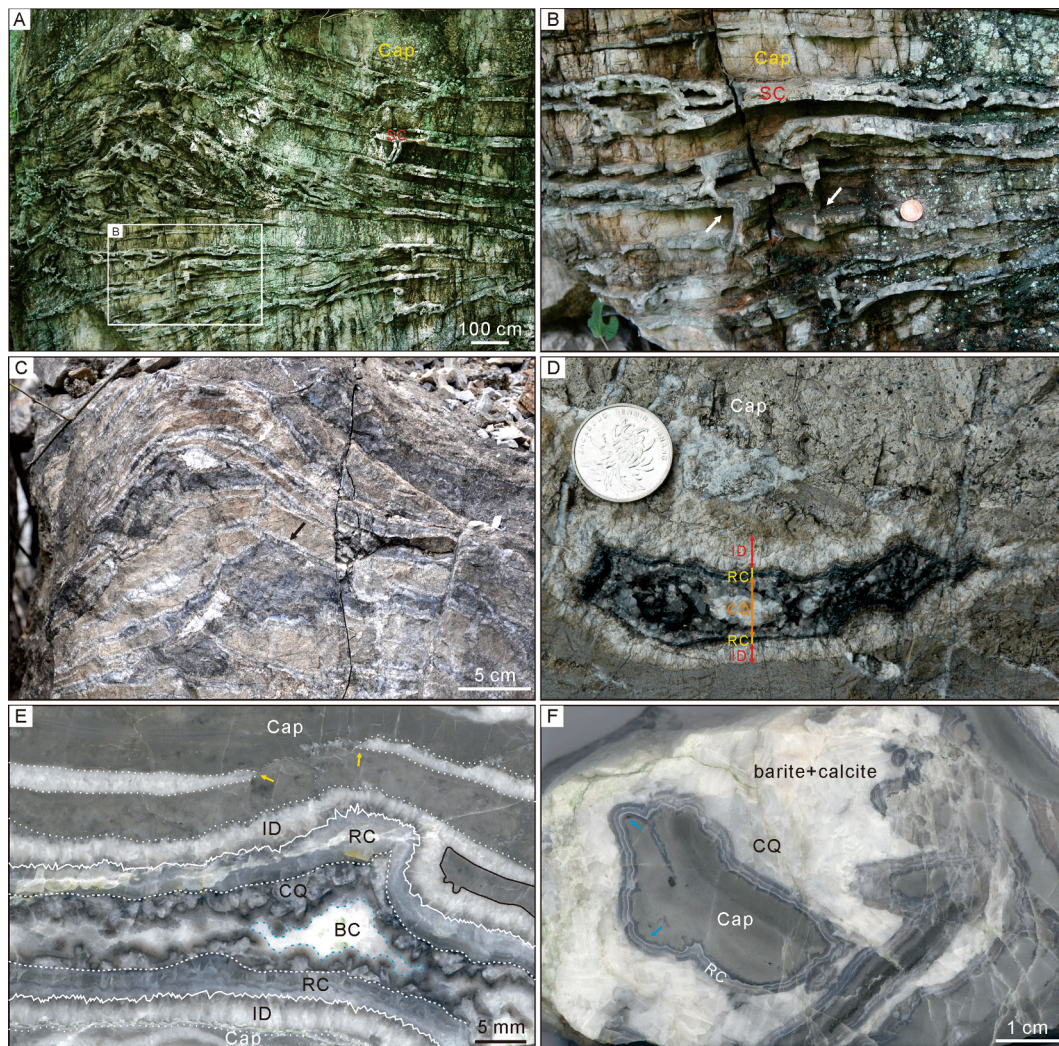


Fig. 3. Field photographs (A–D) and polished slabs (E–F) of sheet-cavity cements in basal Doushantuo cap dolomite. (A) Sheet-cracks from Xiaofenghe section. Sheet-cracks (“SC”) are filled with quartz that is more resistant to weathering than cap dolomite matrix (“Cap”). Note that sheet-cracks can follow and cross-cut sedimentary beds, thus forming a network of cracks. (B) Enlargement of box in (A), showing sharp corners (arrows) of sheet-cracks, suggesting that they were likely opened by physical processes. (C) Sheet-cavities (black arrow) from the Daping section. Sheet-cavities are filled with cements and follow domed beds associated with tepee-like structures. (D–F) Sheet-cavities from Huajipo (D), Daping (E, sample 19DPc1-2), and Beidoushan (F, sample WA-3), filled with multiple generations of cements. Cap, cap dolomite; ID, isopachous dolomite; RC, radial chalcedony; CQ, crystalline quartz; BC, blocky calcite. Small sheet-cavities have sharp terminations (yellow arrows in E) and are filled ID only, whereas larger ones have multiple generations of cements including ID, RC, CQ, and BC. Solid and dotted lines mark boundaries between cap dolomite and multiple generations of cements. Blue arrows in (F) denote smoothed or rounded boundary between RC and a breccia of the cap dolomite. The ID in (F) is too thin to be visible at this scale. Coin in (B) is 19.1 mm in diameter and in (D) is 22.3 mm. (For interpretation of the references to color in this figure legend, the reader is referred to the web version of this article.)

(e.g., Beidoushan section), the isopachous dolomite is thin and hardly recognizable, even in large sheet cavities (Fig. 3F). In some upper slope sections (e.g., Daping section), sheet-cavities have sharp terminations (Fig. 3E, yellow arrows), suggesting limited dissolution of the cap dolomite and the dominance of physical processes in opening up the sheet-cracks, whereas in the outer shelf Beidoushan section, breccias of cap dolomite have smooth margins (Fig. 3F, blue arrows), indicating that they may have been rounded by chemical dissolution.

Isopachous dolomite typically consists of a layer of isopachous radial dolomite, with a variable thickness of 0–5 mm. Dolomite crystals in isopachous dolomite are typically euhedral and columnar (~100–400 μm in width and ~800–1500 μm in length) with sharp rhombic terminations pointing toward the center of sheet-cavities (Fig. 4A–C, 4E), indicating nucleation on sheet-cavity walls and crystal growth toward sheet-cavity center. In cross-polar microscopy, these columnar crystals exhibit uniform extinction and length-slow optical characters, indicating that the crystals were probably precipitated as primary dolomite

(Hood and Wallace, 2012; Hood et al., 2015; Wallace et al., 2019). Back scattered electron SEM observation revealed the presence, at the contact between isopachous dolomite and cap dolomite matrix, of a thin (10–50 μm) layer of material enriched in pyrite and clay minerals (blue arrow in Fig. 4D). This observation is further confirmed by μXRF elemental mapping, which revealed the enrichment of K, Al, and S at the contact between isopachous dolomite and cap dolomite matrix (arrows in Fig. 5F–H), indicating the presence of illite and pyrite, perhaps as dissolution residues and authigenic minerals, respectively. Under cathodoluminescence (CL) microscopy, isopachous dolomite exhibits bright luminescence with dull to non-luminescent growth bands (Fig. 4E), probably due to changing Fe/Mn ratios and redox condition of sedimentary fluids, consistent with μXRF elemental maps of Fe and Mn (Fig. 5L–M). The CL image clearly illustrates that isopachous dolomite crystals terminate toward the center of sheet-cavities.

Isopachous fibrous calcite typically overlies isopachous dolomite and is best seen at the Xiaofenghe, Jiulongwan, Huajipo, and Daping

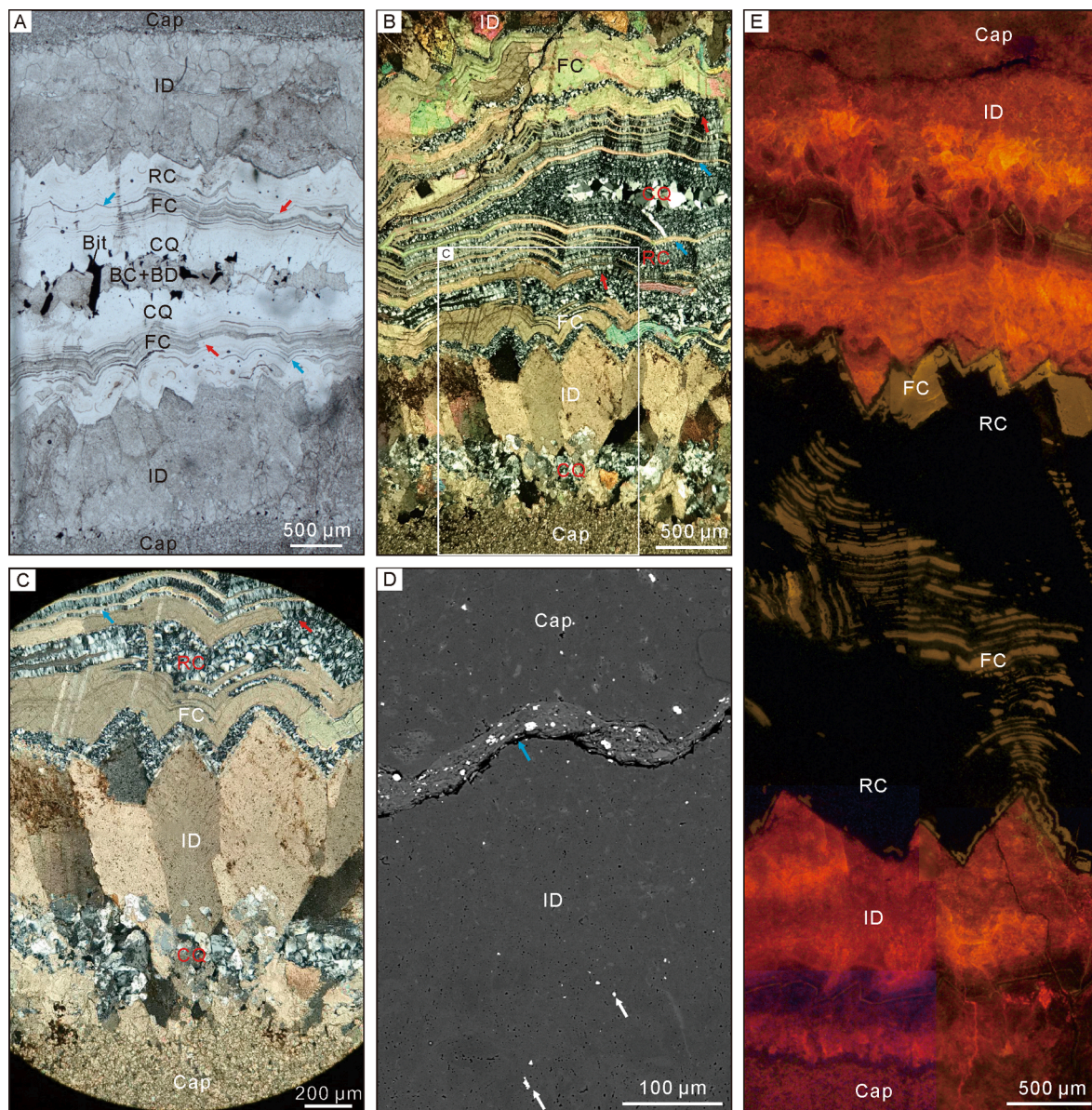


Fig. 4. Petrographic thin sections of multiple generations of cements in sheet-cavities in Doushantuo cap dolostone. (A–C) Plane-polarized light microscopic image (PPL, A) and cross-polarized light microscopic images (XPL, B–C), showing the relationship between cap dolomite (“Cap”), isopachous dolomite (“ID”), fibrous calcite (“FC”), radial chalcidony (“RC”), crystalline quartz (“CQ”), blocky calcite (“BC”), blocky dolomite (“BD”), and bitumen (“Bit”) in sheet-cavities. Red arrows denote secondary replacement of FC by RC. Blue arrows denote residual FC in partially silicified FC laminae. (C) Enlargement of box in (B). Note that ID is also partially silicified (label “CQ” in the lower part of B and C). (D) Secondary electron (SE) scanning electron microscopic (SEM) photomicrograph showing the enrichment of clay minerals and pyrite at the contact between cap dolostone and ID (blue arrow). White arrows denote disseminated pyrite in ID. (E) Cathodoluminescence (CL) microscopic photomicrograph showing ID with bright orange luminescence and dull non-luminescent bands. Note residual FC laminae and non-luminescent RC. (A) is from Huajipo (sample HJP-CL-2.4); (B–C, E) are from Xiaofenghe (B–C, sample XF/2.5; E, sample XFH-4); (D) is from Daping (sample 19DPc1-3). (For interpretation of the references to color in this figure legend, the reader is referred to the web version of this article.)

sections. Fibrous calcite can be up to 700 μm thick and consists of alternating isopachous fibrous laminae that are 20–70 μm in thickness. Fibrous calcite laminae inherit the topographic relief of the underlying isopachous dolomite crystals but become progressively flattened towards the cavity center (Fig. 4A–C, 4E). There does not seem to be any significant dissolution at the contact between isopachous dolomite and fibrous calcite because isopachous dolomite crystals retain their sharp terminations (Fig. 4A–C, 4E), suggesting that there had not been a significant time lag between isopachous dolomite precipitation and fibrous calcite precipitation. In our samples, some fibrous calcite laminae are silicified to become radial chalcidony fabrics to be described below. In cases of partial silicification, fibrous calcite laminae alternate with radial chalcidony laminae (Fig. 4A–C, 4E, 5). Fibrous calcite laminae

can be abruptly truncated by and laterally transition to siliceous radial chalcidony laminae (red arrows in Fig. 4A–C; Fig. 4E; black arrows in Fig. 6A–C), and radial chalcidony is typically fabric destructive (i.e., laminae are poorly preserved or not retained at all; Fig. 4A–C, 4E, 6A–C). Under CL microscopy, residual fibrous calcite is dark brown in color whereas radial chalcidony is non-luminescent (Fig. 4E).

Siliceous phases include isopachous radial chalcidony and crystalline quartz fabrics. Radial chalcidony laminae (ca. 1–4 mm in thickness) are isopachous chalcidony lining on the walls of sheet-cavities or coating on breccias in sheet-cavities (Fig. 4A–C, 4E, 5, 6A–C, 7). In most cases, they directly overlie isopachous dolomite crystals and sometimes contain a variable amount of organic matter. As discussed above, radial chalcidony likely represents silicified fibrous calcite.

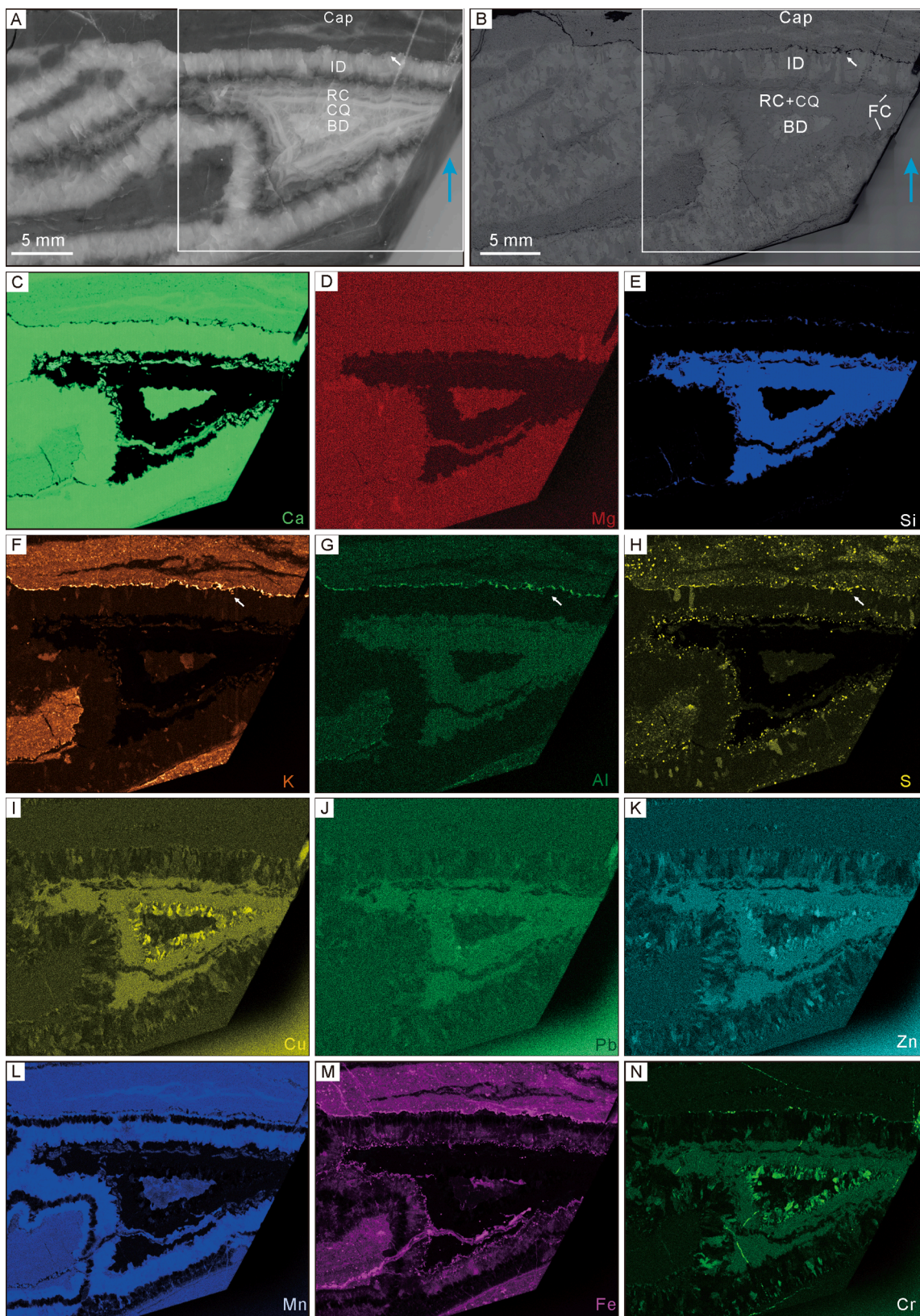


Fig. 5. Polished rock slabs and corresponding μ XRF elemental maps. (A–B) Scanned image (A) and reflected light microscopic photomicrograph (RLM; B) of the same specimen, showing multiple generations of cements in sheet-cavities. White boxes correspond to μ XRF elemental maps (C–N). Blue arrows denote stratigraphic up direction. (C–N) Elemental maps. Elements are marked in the lower right. White arrows in A, B, F, G, and H mark enrichment of K, Al, and S in a thin layer between ID and cap dolostone, possibly because of the presence of illite and pyrite. Specimen is from Daping (sample 19DP2-2z). See Fig. 4 for cement abbreviations. (For interpretation of the references to color in this figure legend, the reader is referred to the web version of this article.)

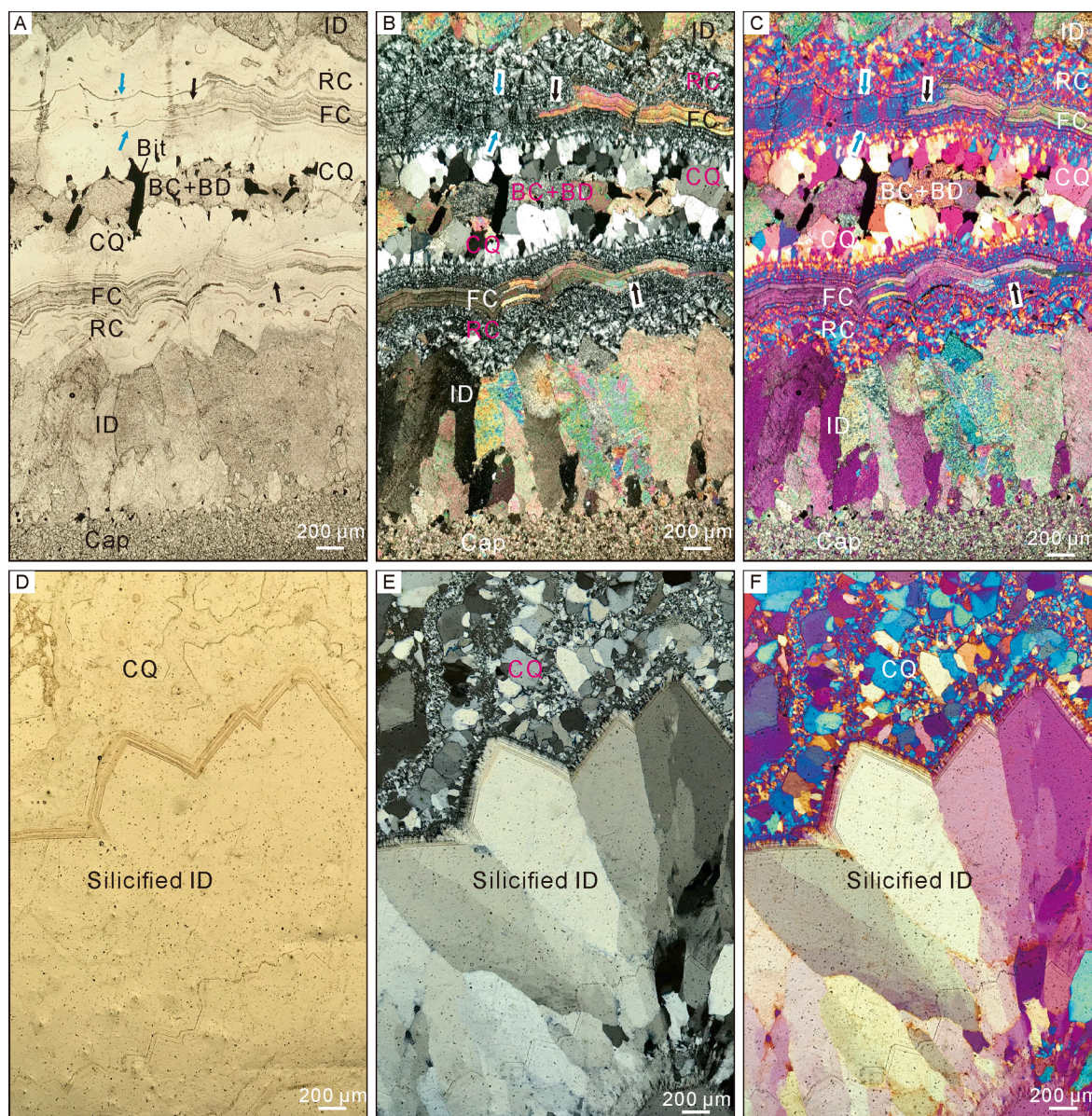


Fig. 6. Petrographic thin sections of sheet-cavities in Doushantuo cap dolostone in South China, showing multiple generations of cements. (A–C) Photomicrographs of the same area showing partial replacement of FC by RC. Also illustrated in Fig. 4A. Black arrows denote FC laminae replaced by RC, and blue arrows denote palimpsest organic-rich laminae, although most laminae have been destroyed by silicification. (D–F) Photomicrographs of the same area showing pervasive silicification. Few laminae are retained in CQ fabrics, although crystal terminations are preserved in silicified ID. Photomicrographs are taken under PPL (A, D), XPL (B, E), and XPL with a 530 nm accessory plate (C, F). (A–C) are from Huajipo (sample HJP-CL-2.4). (D–F) are from Tianjiayuanzi (sample QBN-003). See Fig. 4 for cement abbreviations. (For interpretation of the references to color in this figure legend, the reader is referred to the web version of this article.)

Crystalline quartz consists of sub-euhedral to euhedral crystals (ca. 20–700 μm in size) and typically overlie radial chalcidony. Like radial chalcidony, crystalline quartz is probably also a replacement phase, as it can be seen partially replacing isopachous dolomite (Fig. 4B–C) or pervasively replacing isopachous dolomite crystals (Fig. 6D–F). However, we cannot exclude the possibility that some crystalline quartz was precipitated in free cavity space or represents a phase replacing the blocky calcite fabrics as described below (e.g., Fig. 6A–C). Elemental maps based on μXRF show that both siliceous phases (radial chalcidony and crystalline quartz) are enriched in Si, Al, Cu, Pb, Zn, and Cr but depleted in Ca, Mg, K, Mn, and Fe (Fig. 5) relative to the cap dolostone and isopachous dolomite.

Blocky calcite mainly consists of dark- to light-gray equant calcite crystals, which usually occlude the residual pore space after the siliceous phases (Fig. 3E–F, 4A, 6A–C, 7A, 7C), although sometimes there is still

residual pore space in the sheet-cavity after blocky calcite precipitation. At Beidoushan, Daping, Xiaofenghe, and Huajipo, there are also blocky dolomite and/or barite crystals associated with blocky calcite (Fig. 3F, 4A, 5, 6A–C). At multiple localities in South China, extremely negative $\delta^{13}\text{C}_{\text{carb}}$ values have been acquired from dark-gray blocky calcite in sheet-cavities (Bristow et al., 2011; Jiang et al., 2003; Wang et al., 2008; Wang et al., 2017).

Pyrite is a minor phase in sheet-cavities of Doushantuo cap dolostone. Fine anhedral and euhedral pyrite crystals are sparsely disseminated in isopachous dolomite, particularly at the contact between isopachous dolomite and the cap dolostone (Fig. 4D). Euhedral pyrite crystals (10–150 μm but mostly 30–70 μm in crystal size) occur as bands (Fig. 7A), and fine pyrite crystals can be found in the thin laminae of radial chalcidony fabric (Fig. 7B). Finally, medium- to coarse-grained euhedral pyrite (crystal size of 200–500 μm) coats on fragments of

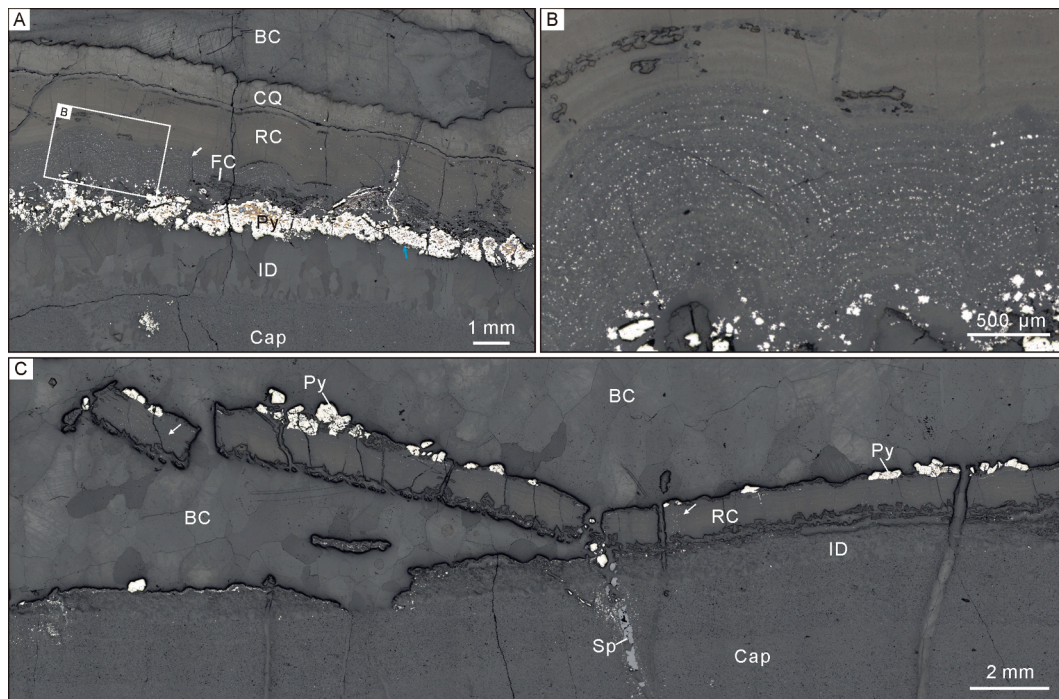


Fig. 7. Petrographic thin sections of sheet-cavities in Doushantuo cap dolostone in South China, showing distribution of pyrite. (A) RLM photomicrograph showing layer of coarse-grained pyrite (“Py”) capping ID (blue arrow), and fine-grained pyrite along laminae in RC (white arrow). (B) Enlargement of box in (A), showing laminae of fine-grained pyrite in RC. (C) RLM photomicrograph showing a sphalerite (“Sp”) vein and pyrite coating (“Py”) on fragments of RC. Arrows point to fine-grained pyrite in RC. (A–B) are from Daping (sample 19DP2-2D). (C) is from Jiulongwan (sample 19JLW-12). See Fig. 4 for cement abbreviations.

radial chalcedony fabric (“Py” in Fig. 7C), and euhedral sphalerite occurs as veins in the cap dolomite (Fig. 7C).

6. Description of speleothem-like structures in sheet-cavities

Fibrous calcite and radial chalcedony fabrics in sheet-cavities can form distinct structures, most of which consist of completely silicified radial chalcedony, but some are partially silicified, with residual calcite laminae still visible (Figs. 4–6). These structures are described below under six morphological types (Figs. 8–12).

Pendant columnar structures hanging downwards from the ceiling of sheet-cavities were observed at Beidoushan, Wenghui, and Tianjiayuanzi (Fig. 8, 9A, 9D, 9F, 10A–B). They occur as singular or coalesced columns. Individual columnar structures are 2–8 mm in diameter and 3–30 mm in length. They typically contain a straight central tube (red arrows in Fig. 8, 9D, 9F, 10A–B), which is ~ 100 μm in diameter and filled with chalcedony. The central tube is surrounded by radial chalcedony laminae delineated by organic-rich layers (Fig. 8B–D). Some of these laminae appear botryoidal in shape (Fig. 8B–C), and the outermost laminae are typically thicker (100–200 μm) than the inner ones (30–70 μm) (Fig. 8B–C).

Pillar-like structures rising from the floor of sheet-cavities were observed at Wenghui, Xiaofenghe, and Beidoushan (Fig. 9A–B, 9D–E, 10C). Different from the pendant columnar structures described above, these structures lack a straight central tube. They taper distally, with a diameter of ca. 5–13 mm and a length of ca. 10–35 mm. In longitudinal sections, they begin as stacked mamillary structures (arrows in Fig. 9B), and later growth is characterized by continuous, smooth, and alternating organic-rich and organic-poor laminae each 20–40 μm in thickness and ~ 2 mm in total thickness (Fig. 9B–C). In one example, a columnar structure extends from the ceiling to the floor of the sheet-cavity (Fig. 8A). Although most pillar-like structures are composed of radial chalcedony, those from Xiaofenghe consist of a mixture of radial

chalcedony and fibrous calcite (Fig. 10C), representing partial silicification of fibrous calcite, as discussed in section 5.

Irregular ramiforms growing obliquely rather than vertically, often with branches and sometimes bends (Fig. 11A–B), were found in sheet-cavities at Beidoushan. They are typically ca. 1–2 mm long and 200–300 μm wide. A narrow central tube 10–20 μm in diameter is present in some ramiform structures (arrows in Fig. 11B). They typically consist of an inner zone (50–100 μm wide) of homogenous cement and an outer zone (50–80 μm wide) of laminae enriched in clay and organic matter (Fig. 11A–B).

Tubercular forms characterized by extremely fine crystals forming laterally continuous crusts on the walls of sheet-cavities were found at Beidoushan (Fig. 11C–D). They typically consist of a microcrystalline quartz core (a few mm thick) and an outer shell (~500 μm thick) with alternating organic-poor and organic-rich chalcedony laminae. Filamentous microfossils are sometimes preserved in the microcrystalline core (Fig. 11C–D, arrows) (Gan et al., 2021).

Botryoidal structures are found in Doushantuo sheet-cavities at Zhangcunping, Beidoushan, and Daping (Fig. 12A–G). They mainly consist of coalesced hemispherical to nodular protuberances up to 5 mm in size. Typically, a botryoid starts with a clotted aggregate that is covered with alternating organic-rich and organic-poor laminae (Fig. 12D–G). Partially silicified laminae indicate that they were originally calcareous (Fig. 12E–F).

Finally, flat microlaminated structures here described as flat crusts are common in Doushantuo sheet-cavities at Beidoushan, Wenghui, and Xiaofenghe (Fig. 8A, 9A–C, 11A, 12H–I). They are typically ca. 0.1–10 mm thick and consist of alternating organic-poor and organic-rich chalcedony laminae each ~ 20–60 μm thick (Fig. 9C, 11A, 12H–I). They sometimes transition laterally to pendant columnar structures (Fig. 8A, 9A), pillar-like structures (Fig. 9A–B), and irregular ramiforms (Fig. 11A).

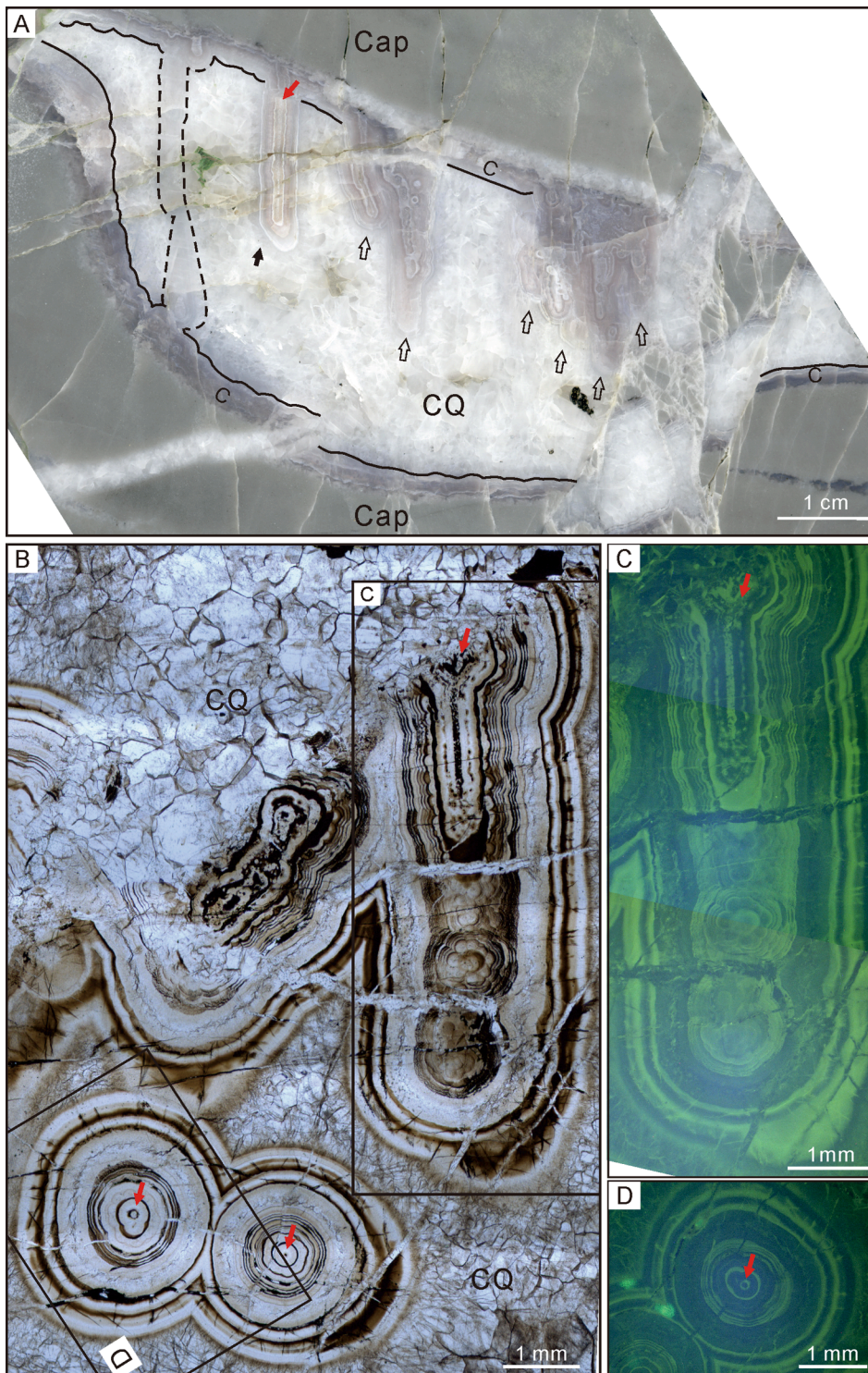


Fig. 8. Polished slab and thin section of silicified speleothems in sheet-cavities in Doushantuo cap dolostone at Beidoushan. (A) Polished slab, showing flat crust (labeled “C” and outlined by black lines), singular stalactite (solid black arrow), with “soda-straw” drip channel marked by red arrow), coalesced stalactites (hollow black arrows), a stalagnate (where a stalactite meets a stalagmite, dashed lines), and CQ between speleothems. (B) PPL image of thin section, showing transverse and longitudinal sections of stalactites with “soda-straw” drip channels (red arrows). (C–D) Epifluorescence light microscopic (ELM) images of areas marked in (B) showing “soda-straw” drip channels (red arrows), bright organic-rich laminae, and dull organic-poor laminae. (A–D) are from Beidoushan (A, sample 18BDS-2; B–D, sample 18WA-6d). See Fig. 4 for cement abbreviations. (For interpretation of the references to color in this figure legend, the reader is referred to the web version of this article.)

7. Discussion

7.1. Interpretations and origins of speleothem-like structures

The origins of sheet-cavity cements (including isopachous dolomite, fibrous calcite, radial chalcidony, crystalline quartz, blocky calcite, and blocky dolomite) have been a subject of continuing debate (Cui et al., 2019; Zhou et al., 2010; Zhou et al., 2017b). Below we consider and evaluate several possible interpretations.

7.1.1. Marine and early diagenetic cementation

Marine cementation has been reported from sheet-cracks in cap dolostones overlying the Sturtian and Marinoan diamictites in the Adelaide Geosyncline of South Australia (Wallace et al., 2019). Wallace et al. (2019) argued that these sheet-cracks formed as a result of volume expansion related to dolomitization near the seafloor. Hence, dolomite precipitates within these sheet-cracks are interpreted as marine cements, and this interpretation is supported by petrographic observations, such as the presence of internal sediment within the sheet-cracks and the length-slow optic nature of isopachous dolomite cement in the

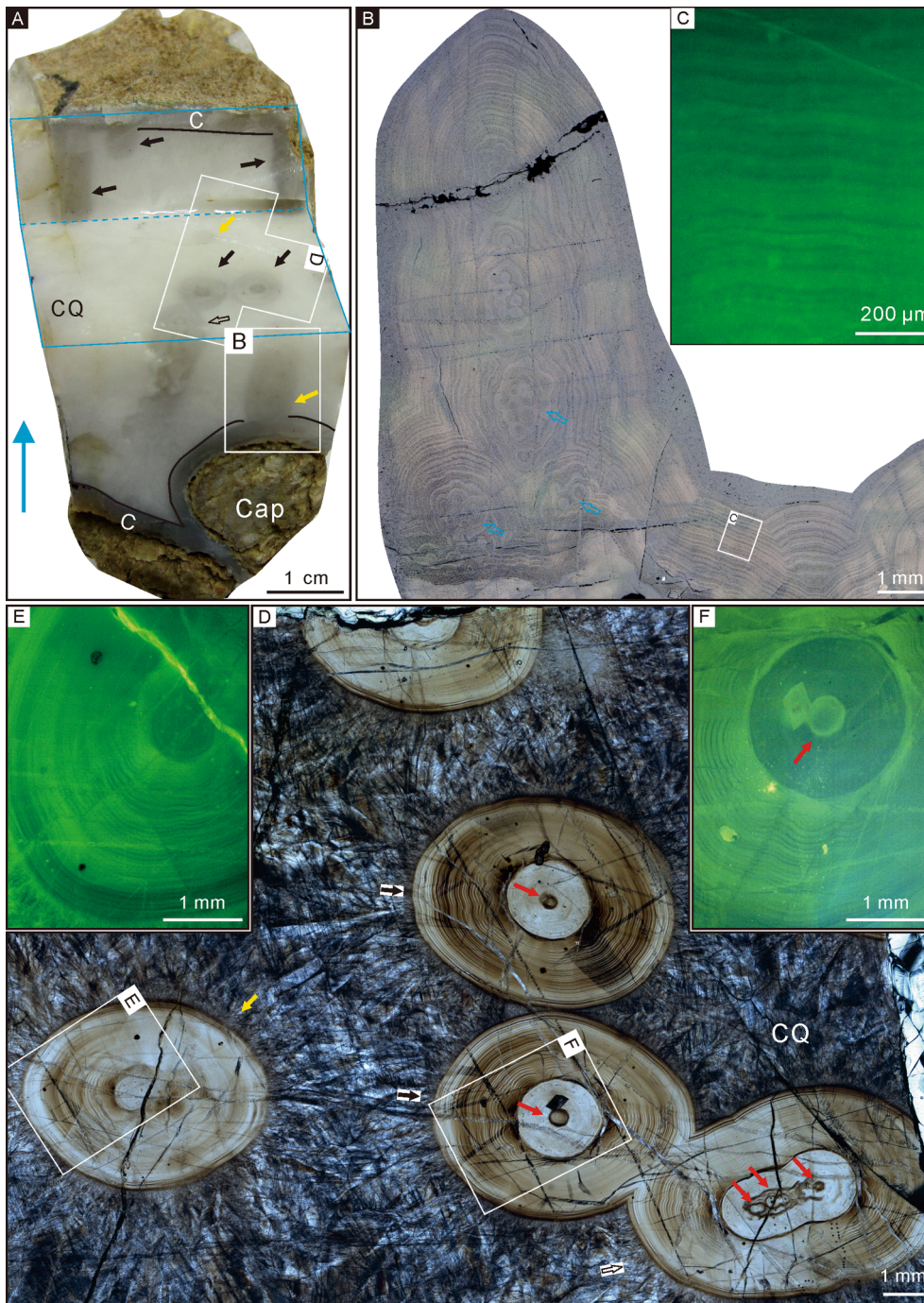


Fig. 9. Hand specimen and thin sections of silicified stalagmites, stalactites, and flat crusts in sheet-cavities of Doushantuo cap dolostone. (A) Stratigraphically oriented hand specimen with three cut surfaces (one horizontal and two vertical cuts that together resemble a staircase), showing stalagmites (yellow arrows), singular and coalesced stalactites (solid and hollow black arrows, respectively), and flat crust (labeled “C” and marked by black lines). Stratigraphic up direction on top (blue arrow). Blue lines outline two orthogonal cut surfaces (analogous to the step and riser of a staircase), highlighting the horizontal and vertical cross-sections of vertically oriented stalagmites and stalactites. (B) RLM image corresponding to the labeled rectangle in (A), showing a stalagmite with mamillary aggregates (hollow blue arrows) and FC. (D) PPL image corresponding to the area marked in (A) showing stalagmite (yellow arrow), singular and coalesced stalactites (solid and hollow black arrows, respectively), “soda-straw” drip channel (red arrows), and crystalline quartz (CQ) between paleospeleothems. (C, E, F) ELM images corresponding to labeled rectangles in (B) and (D), showing alternating bright organic-rich and dull organic-poor laminae, as well as a “soda-straw” drip channel (red arrow in F). (A–F) are from Wenghui (sample 16WH-2). See Fig. 4 for cement abbreviations. (For interpretation of the references to color in this figure legend, the reader is referred to the web version of this article.)

sheet-cracks. Wallace et al.’s (2019) interpretation of marine cementation may be applicable to the first generation of cements in Doushantuo sheet-cavities, i.e., the isopachous dolomite, which also consists of length-slow dolomite crystals and has geochemical signatures similar to those of the Doushantuo cap dolostone (Zhao et al., 2018; Zhou et al., 2010). However, the multiple generations of cements that grow centripetally in Doushantuo sheet-cavities indicate that they represent void-filling cements; in other words, the precipitation of isopachous dolomite and later cements postdates the formation of sheet-cavities and the brecciation/dissolution of the cap dolostone (Fig. 3F). Importantly, the pillar-like structures and particularly the pendant columnar structures with a straight central tube, which are described in section 6, cannot be easily reconciled with marine cementation. Additionally, the lack of any internal sediment (e.g., dolomicrite) in Doushantuo sheet-

cavities is inconsistent with marine cementation, as internal sediment would be introduced to the cavities in high-energy subtidal-intertidal environments (Haas, 2004).

Gammon and colleagues argued that the sheet cracks in the basal Ediacaran cap dolostone of the Nuccaleena Formation in the Adelaide Geosyncline of South Australia were generated by pore-fluid overpressurization, and these cracks were filled by early diagenetic dolomite and calcite precipitation fueled by fluid convection and diffusion through the network of sheet-cracks (Gammon, 2012; Gammon et al., 2012). While we agree that pore-fluid overpressurization may have contributed to the formation of Doushantuo sheet-cavities, and that the isopachous dolomite in Doushantuo sheet-cavities may be early diagenetic or even marine cements (Zhou et al., 2010), we find that the early diagenetic model does not provide a satisfactory explanation for the

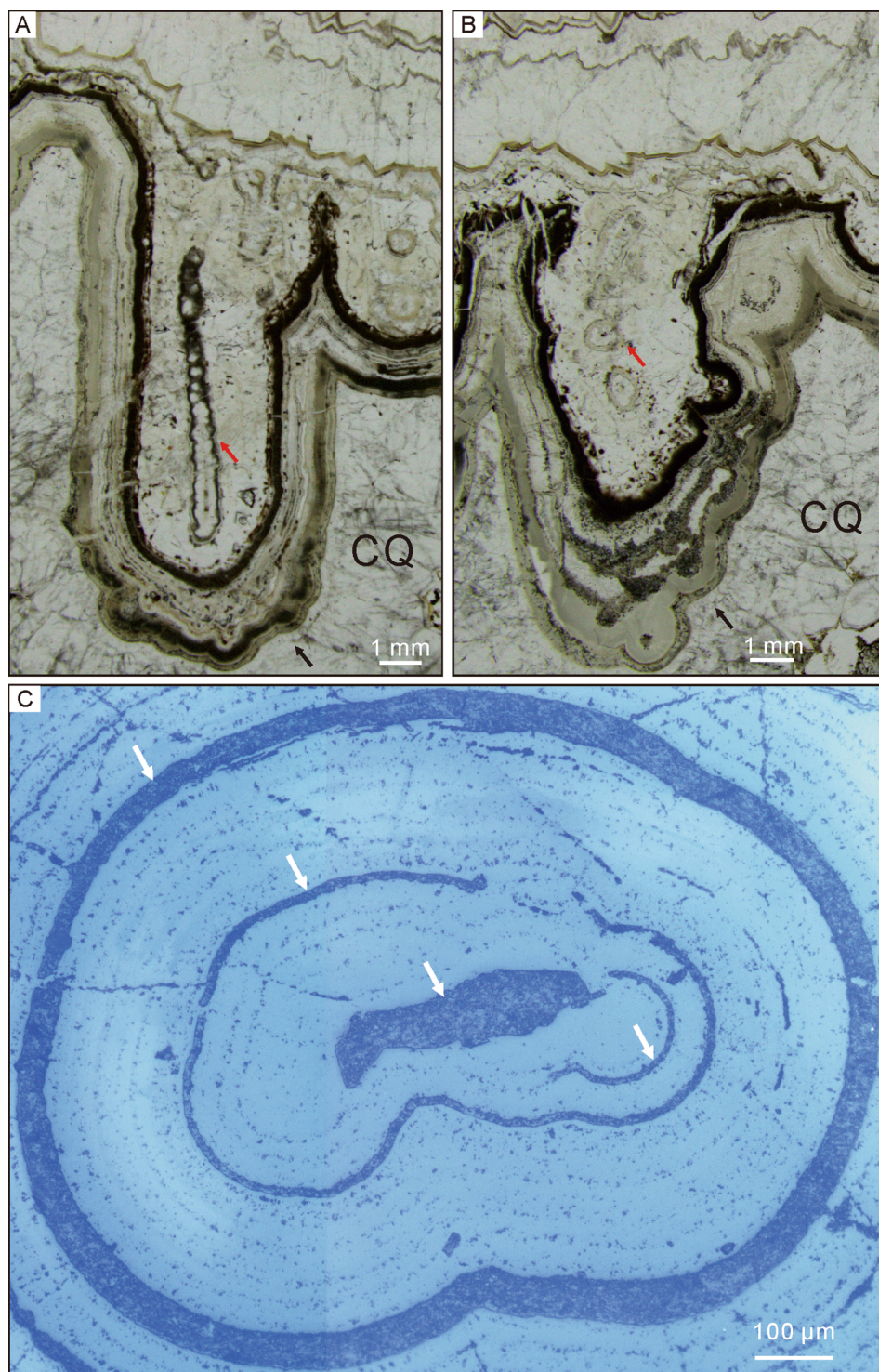


Fig. 10. Thin sections of silicified speleothems in sheet-cavities in Doushantuo cap dolostone. (A–B) PPL images showing a longitudinal section of stalactites (black arrows) with “soda-straw” drip channels (red arrows). (C) RLM image of a transverse section of a partially silicified stalagmite with residual calcite laminae (white arrows). (A–B) are from Tianjiayuanzi (sample RVS-1) and (C) is from Xiaofenghe (sample 14XFH-7). See Fig. 4 for cement abbreviations. (For interpretation of the references to color in this figure legend, the reader is referred to the web version of this article.)

pillar-like structures and the pendant columnar structures with a straight central tube, which are found in the Doushantuo sheet-cavities.

7.1.2. Hydrothermal origin

The precipitation of siliceous phases of cements (i.e., radial chalcedony and crystalline quartz) in Doushantuo sheet-cavities may have been influenced by hydrothermal activities because their positive Eu anomalies and Ge/Si ratios suggest contributions from hydrothermal fluids (Cui et al., 2019), and also because fluid inclusions in crystalline quartz have homogenization temperatures of 160–220 °C (Zhou et al.,

2017b). This interpretation, as discussed further below, is plausible. However, radial chalcedony and crystalline quartz are replacement phases of isopachous dolomite, fibrous calcite, and perhaps blocky calcite/dolomite (Fig. 4A–C, 4E, 6, 12E–F). Thus, they post-date the calcareous phases and do not mandate a hydrothermal origin for the latter phases. Furthermore, a hydrothermal origin does not account for the straight central tube in the pendant columnar structures in the Doushantuo sheet-cavities.

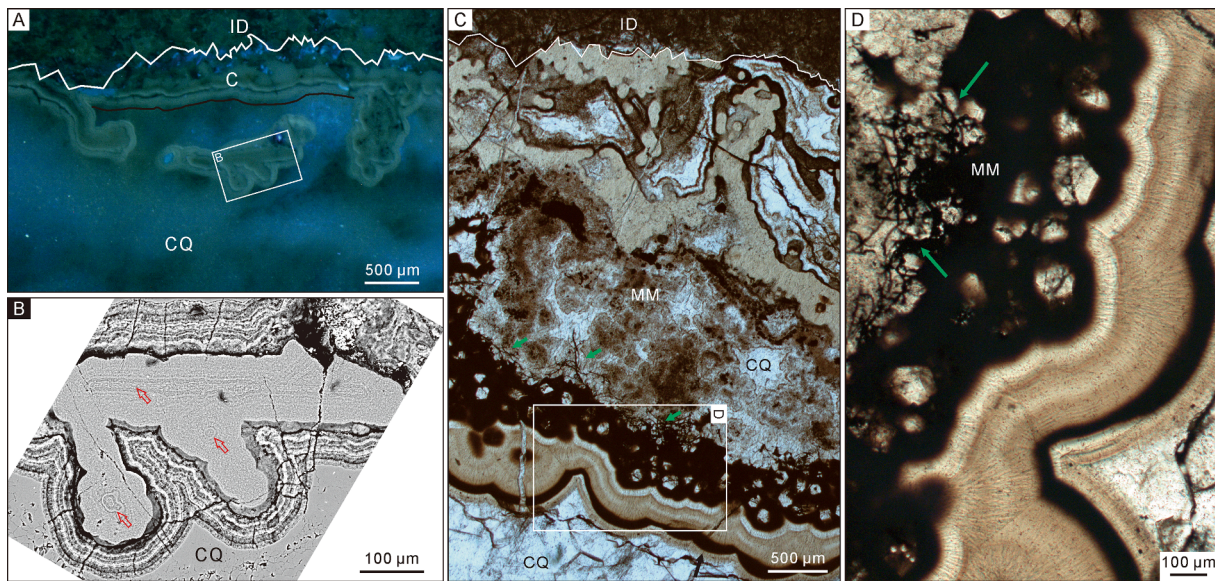


Fig. 11. Thin sections of silicified helictites, moonmilk, and flat crust in sheet-cavities of Doushantuo cap dolostone. (A) ELM image showing isopachous dolomite (labeled “ID”), flat crust (labeled “C”), and vermiform helictites. (B) Backscattered scanning electron microscopic (BSEM) image of the labeled rectangle in (A), showing helictite with barely discernible central canals in longitudinal section (upper arrow) and transverse sections (lower arrows). (C) PPL image showing ID, CQ, and moonmilk (“MM”). (D) Enlargement of the labeled rectangle in (C), showing filamentous microfossils (green arrows in C and D). (A–D) are from Beidoushan (A–B, sample 18BDS-9; C–D, sample 18BD-12). See Fig. 4 for cement abbreviations. (For interpretation of the references to color in this figure legend, the reader is referred to the web version of this article.)

7.1.3. Speleothems

Based on their morphological similarity to modern speleothems (Banks and Jones, 2012) and their close association with a karstic surface atop the Doushantuo cap dolostone, the six types of speleothem-like structures described in section 6 are best interpreted as paleo-speleothems (Table 1).

The pendant columnar structures are interpreted as stalactites (Fig. 8, 9A, 9D, 9F, 10A–B). Laminae in these pendant structures, like growth bands in stalactites, reflect chemical changes of drip-water perhaps due to seasonality (Frisia et al., 2003). Dark organic-rich laminae are similar to dark bands in modern stalactites that contain exogenous organic material (Frisia et al., 2003) or host biofilms (Jones, 2011). Some of these laminae appear botryoidal in shape (Fig. 8B–C), reflecting stable and slow feeding of drip water. A straight central tube (red arrows in Fig. 8, 9D, 9F, 10A–B) is a common feature (known as “soda-straw”) in modern stalactites, where water is drawn inside the tube and drip at the tip (Fairchild et al., 2006). Thus, the pendant structures are morphologically similar to modern stalactites and are here interpreted as ancient stalactites.

The pillar-like structures are interpreted as stalagmites (Fig. 9A–B, 9D–E, 10C). Modern stalagmites typically lack a “soda-straw” drip channel (Fig. 9A–B, 9D–E, 10C), taper distally, and have round tops. These features are also present in the pillar-like structures. The pillar-like structures are millimeter-centimeter in size, thus representing “minimum-diameter” stalagmites (Fairchild and Baker, 2012) in microkarst cavities where drip fall heights were short; this interpretation is consistent with the small size of the Doushantuo sheet-cavities relative to modern karstic caves. Stacked mamillary structures (Fig. 9B) are typically observed at the bottom of modern stalagmites (Baker et al., 1993) and represent turbulence of drip water at the beginning of stalagmite deposition (Dreybrodt and Romanov, 2008). Later growth laminae are more continuous and smoother, as found in modern calcareous stalagmites (Baker et al., 1993). The columnar structure that extends from the ceiling to the floor of the sheet-cavity (dash line in Fig. 8A) likely represents a stalagmite and a stalactite meet and grow together (Gribovski et al., 2017).

The ramiform structures are interpreted as helictites based on their

irregular orientation with random branches and bends (Fig. 11A–B). The central tube in some ramiform structures (arrows in Fig. 11B) is consistent with the helictite interpretation; some modern helictites do have a central tube that is functionally similar to the “soda-straw” of stalactites and likely reflects the influence of irregular airflow in karstic cavities (White, 2005).

The tubercular structures are interpreted as moonmilk (Fig. 11C–D). This interpretation is based on their similarity to Holocene calcareous moonmilk, e.g., from the Grotta Cesare Battisti cave, Italy (Borsato et al., 2007), which consists of a core of microcrystals with filamentous microbes and a shell of isopachous laminae. It has been proposed that the formation of modern moonmilk may have been facilitated by microbial activities (Baskar et al., 2011; Cañaveras et al., 2006), although some modern moonmilk may be inorganic in origin (Borsato et al., 2007; Jones, 2011). Filamentous microfossils, interpreted as fungus-like micro-organism (Gan et al., 2021), are common in the microcrystalline quartz core of moonmilk in the Doushantuo sheet-cavities at Beidoushan and Datang (arrows in Fig. 11C–D), indicating an intimate relationship between moonmilk formation and micro-organisms, which could have served as nucleation sites for speleothem precipitation.

Doushantuo botryoids are interpreted as botryoidal speleothems (Fig. 12A–G). As modern botryoidal speleothems, they are characterized by laminae of fibrous minerals, and their hemispherical shape is ascribed to fast growth on protrusions of the substrate (Caddeo et al., 2015). Importantly, the residual calcite laminae (Fig. 12E–F) affirm that they were originally calcareous and were secondarily silicified (see discussion in section 5).

The flat crusts are also interpreted as paleo-speleothems (Fig. 8A, 9A–C, 11A, 12H–I). Their fabric is similar to modern flowstone that typically precipitates from flowing water on the floor of karstic caves (Chafetz and Butler, 1980). However, Doushantuo flat crusts sometimes form an isopachous lining on all sheet-cavity walls. Given the small size of Doushantuo sheet-cavities, it is possible that the formation of flat crusts was mainly controlled by evaporation and condensation processes (see discussion in section 7.3).

The speleothem interpretation also raises several questions. These include (1) the temporal and genetic relationship between post-glacial

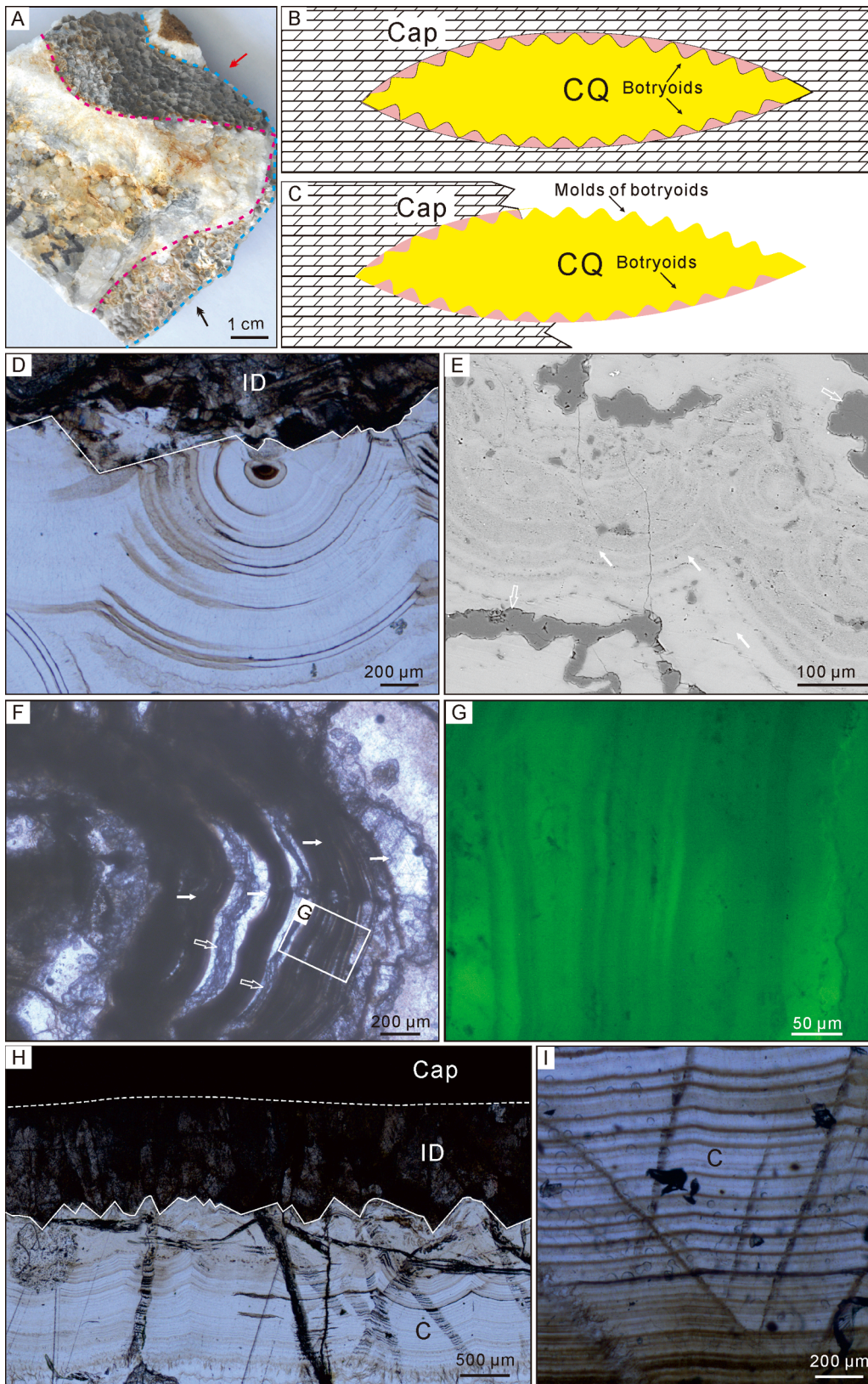


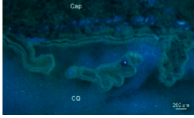
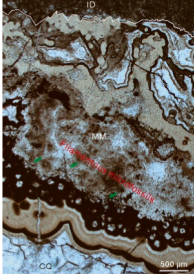

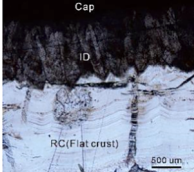


Fig. 12. Hand sample and thin sections of silicified and partially silicified flat crust and botryoids in sheet-cavities of Doushantuo cap dolostone. (A) Hand sample showing molds of botryoids (red arrow) and botryoids (black arrow) in a sheet-cavity filled with cement growing from the upper right and lower right. Red and blue dotted lines mark, respectively, the inner and outer boundaries of botryoids. (B–C) Schematic diagram showing preservation mode of botryoids in (A). Silicified botryoids (pink) are exposed on the upper right side of the sheet-cavity, leaving external molds on CQ (yellow). (D) PPL image of a thin section, showing botryoidal laminae overlying ID. (E) BSEM image of a thin section, showing partially silicified botryoids with calcite laminae (solid white arrows) and siliceous replacement (hollow white arrows). (F) PPL image of a thin section, showing partially silicified organic-rich calcareous botryoidal laminae (solid white arrows) and silicified laminae (hollow white arrows). (G) ELM image of the labeled rectangle in (F), showing bright organic-rich and dull organic-poor laminae. (H) PPL photomicrograph of a thin section, showing cap dolostone ("Cap"), isopachous dolomite ("ID"), and flat crust (labeled as "C"). (I) PPL image of a thin section, showing flat crust laminae (marked as "C"). (A) is from Zhangcunping (sample ZCP-1), (D) is from Beidoushan (sample 18WA-7b), (E–G) are from Daping (sample 19DPc1-2), (H) is from Xiaofenghe (sample 14XFH-1), and (I) is from Wenghui (sample 16WH-9). See Fig. 4 for cement abbreviations. (For interpretation of the references to color in this figure legend, the reader is referred to the web version of this article.)

Table 1

Six-type of fibrous calcite and radial chalcedony structures in sheet-cavities and their interpretation.

Structures	Description	Interpretation	Exemplary pictures
Pendant columnar structures	Pendant structures with a straight central tube in the center; hanging downwards from ceiling of sheet-cavities; ca. 2–8 mm in diameter and ca. 3–30 mm in length	Stalactites	
Pillar-like structures	Pillar-like structures without a straight central tube; rising from floors of sheet-cavities; tapering distally; ca. 5–13 mm in diameter and ca. 10–35 mm in length	Stalagmites	
Ramiform structures	Variable in shape and orientation; with a narrow central tube; ca. 1–2 mm long and 200–300 μm wide	Helictites	
Tuberculiform structures	Tuberculiform structures consisting of a core with microbial filaments (a few μm thick) and an outer shell (~500 μm thick)	Moonmilk	
Hemispherical structures	Hemispherical structures coating on sheet-cavity walls and mainly consisting of numerous rounded protuberances resembling botryoids (5 mm in diameter).	Botryoidal speleothems	
Flat microlaminar structures	Flat or slightly wavy isopachous laminae (ca. 0.1–10 mm thick); laterally transitioning to other structures.	Flat crust	

rebound, karstification, sheet-cavity formation, and speleothem precipitation, (2) the mechanisms of speleothem precipitation and silicification, (3) the biological and environmental implications of Doushantuo speleothems, and (4) the paragenesis of cements in sheet-cavities. These questions will be discussed below.

7.2. Post-glacial rebound, karstification, sheet-cavity formation, and speleothem precipitation are temporally and genetically related

Zhou et al. (2010) proposed three successive events that shaped the Doushantuo cap dolostone in South China: (1) post-glacial transgression and deposition of the cap dolostone; (2) post-glacial isostatic rebound and karstification of the cap dolostone, resulting in a widespread karstic surface atop the cap dolostone; and (3) renewed post-glacial transgression and precipitation of cements in sheet-cavities. The absolute timing of these three events is constrained by the high-precision zircon U-Pb ages. The termination of the Marinoan glaciation and initiation of cap dolostone deposition is constrained by a U-Pb zircon age of 634.57

± 0.88 Ma from the topmost Nantuo diamictite (representing the Marinoan glaciation) in South China (Zhou et al., 2019). A U-Pb zircon age of 635.23 ± 0.57 Ma from a tuffaceous bed just above the Doushantuo cap dolostone (Condon et al., 2005) provides a geochronological constraint on the end of cap dolostone deposition and karstification. These two ages bracket the duration of cap dolostone deposition and karstification to be $< 10^6$ yr (Zhou et al., 2019). Additionally, a U-Pb zircon age of 632.50 ± 0.48 Ma from lower Member II of the Doushantuo Formation (Condon et al., 2005) further constrains the karstification event to be > 632 Ma.

Our study confirms the existence of a widespread karstification event after the deposition of the Doushantuo cap dolostone (Zhou et al., 2010). This event generated a karstification surface with a topographic relief of up to 2 m at the top of the cap dolostone. This karstification surface can be observed at multiple sections in South China, possibly because the rapid deposition of thick diamictites during the snowball Earth had primed South China for a strong post-glacial isostatic rebound. Although

the instantaneous gravitational attraction effect of retreating glaciers may also cause a sea-level fall (Hoffman and Macdonald, 2010), the time scale needed for chemical dissolution to generate a karstic surface with a topographic relief of 2 m (Fig. 2) means post-glacial isostatic rebound was the main driver of the local sea-level fall in South China.

Our study also warrants modification of certain aspects of the Zhou et al. (2010) model. Zhou et al. (2010) did not explicitly discuss the origin of Doushantuo sheet-cavities, although others argued that the sheet-cracks were formed physically as a result of an increase in pore-fluid pressure (Corkeron, 2007; Gammon, 2012; Gammon et al., 2012; Jiang et al., 2006) or a decrease in hydrostatic pressure (Hoffman and Macdonald, 2010). Our observation of rounded breccias (Fig. 3F) and the accumulation of clay minerals at the boundary between isopachous dolomite and cap dolostone matrix (Fig. 4D, 5F-H) indicates that chemical dissolution played a role in sheet-cavity formation. Thus, physically initiated cracks may have been augmented by chemical dissolution during isostatic rebound. More importantly, Zhou et al. (2010) argued that cements in sheet-cavities were formed entirely in marine environments during the second transgression, whereas we argue that speleothem precipitation was a subaerial process predating the second transgression. Given the available age constraints described above, our model also implies that post-glacial rebound, karstification, sheet-cavity formation, and speleothem precipitation all occurred within $< 10^6$ years. Thus, we argue that they are genetically related, with post-glacial rebound being the ultimate driver. This interpretation can be further tested by high-resolution in-situ geochemical analysis of fibrous calcite fabrics in speleothem precipitates in the future to examine evidence of meteoric water influence.

7.3. Speleothem precipitation, silicification, and implications for soil microbes

Modern siliceous speleothems can be either primary (Aubrecht et al., 2008) or secondary (Skotnicki and Knauth, 2007). Primary siliceous speleothems may develop in caves or lava tunnels overlain by silicate rocks such as quartzites, sandstones, or igneous rocks (Aubrecht et al., 2008). Although black shale and siltstone overlying the Doushantuo cap dolostone (Fig. 1) could in principle be a silica source, this scenario is inconsistent with the lack of subaerial weathering features in the black shale. Instead, we suggest that the Doushantuo paleo-speleothems were secondarily modified by silicification. In other words, they were originally calcareous paleo-speleothems but later silicified by low-temperature hydrothermal processes. This interpretation is supported by partially silicified Doushantuo paleo-speleothems from Huajipo (Fig. 4A, 6A–C), Xiaofenghe (Fig. 4B–C, 4E, 10C), and Daping (Fig. 5, 12E–F), where residual calcareous laminae are preserved.

Doushantuo paleo-speleothems described here have modern analogs, which include gravitational and non-gravitational speleothems (Banks and Jones, 2012). Gravitational speleothems such as stalactites and stalagmites are related to dripping water sourced from the epikarst. When the dripping water saturated with calcium carbonate flows out of fissures, it degasses and deposits a thin calcite film that contributes to the growth of stalactites and stalagmites (Baker et al., 1993; Railsback et al., 2018; Tan et al., 2013), with alternating laminae representing the fluctuation between affluent and poor feeding or between stable and unstable precipitations (Baker et al., 2002; Brook et al., 1999; Tan et al., 2006). Non-gravitational speleothems include helictites, moonmilk, botryoids, and flat crusts. Helictites may be related to capillary flow driven by changing hydrostatic pressure and airflow (Huff, 1940; Onuk et al., 2014); such capillary flow is too slow to form a hanging droplet. The formation of modern moonmilk is probably driven by microbial-mediated nucleation and mineralization in the crystalline core (Baskar et al., 2011; Cañaveras et al., 2006), followed by relatively slow precipitation of clay-rich or organic-rich laminae in the shell (Borsato et al., 2000; Lacelle et al., 2004); this model is consistent with the presence of filamentous micro-organisms in the core of Doushantuo moonmilk at the

Beidoushan section (Fig. 11C–D) and in radial chalcedony fabrics in general (Gan et al., 2021). Modern analogs of botryoids and flat crusts are mainly controlled by evaporation and condensation processes (Banks and Jones, 2012) rather than drip water, and this may also apply to the Doushantuo counterparts.

Regardless of the types of speleothems, a key process in speleothem precipitation is CO₂ degassing. In modern karstic caves, meteoric water percolates through organic-rich and CO₂-rich soils above caves and becomes progressively acidic groundwater that dissolves carbonate bedrocks. When the CO₂-laden groundwater emerges as drip water in karstic caves, CO₂ degasses and supersaturation drives the precipitation of calcareous speleothems (White, 2005). In other words, an organic-rich soil zone with active CO₂ production is critical for the precipitation of calcareous speleothems (Kaufmann, 2003). In post-Ordovician terrestrial environments, land plants likely played important roles in soil formation and were significant contributors to soil organic carbon, which was respired by soil microbes to produce soil CO₂ (Brasier, 2011; Fairchild et al., 2006; White, 2005). Prior to the rise of embryophytes, however, speleothem precipitation was likely dependent on soil microbes and/or abiotic processes (Brasier, 2011).

We speculate that the precipitation of Doushantuo speleothems was probably facilitated by active soil microbial communities. Pre-Silurian soils were probably thin and had low preservation potential (Algeo and Scheckler, 1998; Retallack, 2003), thus direct paleontological evidence for soil microbes is difficult to come by. However, the preservation of filamentous microfossils in Doushantuo speleothems at the Beidoushan section (Fig. 11C–D) provides evidence for the presence of terrestrial microbes. These microfossils are interpreted, on the basis of their morphological features, as members of the zygomycetes (Gan et al., 2021), which represent a paraphyletic group of terrestrial fungi that include the Mucoromycota and Zoopagomycota (Spatafora et al., 2016). Molecular clock analyses also suggest that terrestrial fungi, including Mucoromycota and Zoopagomycota, had diverged by the Ediacaran Period (Chang et al., 2021; Lutzoni et al., 2018). Fungi are heterotrophic organisms depending on organic carbon produced by autotrophs. We note that early fungi, particularly if they were phagotrophic (Berbee et al., 2020), could have in principle fed on fossil organic carbon derived from sedimentary rocks. However, fossil organic carbon is generally recalcitrant and unlikely to support rapid growth. Furthermore, zygomycetes are osmotrophic and their growth requires cytoplasmic uptake of nutrients that are derived from extracellular enzymatic digestion of microbes, algae, or plants (Berbee et al., 2020). Thus, terrestrial zygomycete fossils from the Doushantuo Formation (Gan et al., 2021) and molecular clock evidence for Ediacaran terrestrial fungi (Chang et al., 2021; Lutzoni et al., 2018) imply the presence of a terrestrial microbial ecosystem capable of colonizing soils and driving speleothem precipitation.

Abiotic processes may have also aided the precipitation of Doushantuo speleothems, as they do in the precipitation of modern speleothems. Brasier (2011) identified a number of abiotic processes that may have contributed to the precipitation of pre-Silurian non-marine carbonates, including speleothems (Brasier, 2011). Among these, perhaps small-scale turbulence flow, temperature change in karstic cavities, and evaporation may have promoted CO₂ degassing and speleothem precipitation in the Doushantuo Formation.

7.4. An integrative paragenesis model of sheet-cavity cementation

7.4.1. Origins of sheet-cavity cements

The origins of isopachous dolomite, fibrous calcite, radial chalcedony, crystalline quartz, blocky calcite, and blocky dolomite have been a subject of continuing debate. Zhou et al. (2010) argued that isopachous dolomite precipitation occurred after karstification and during the second transgression. However, our study shows that isopachous dolomite predates speleothems and both precipitated during the karstification event.

The siliceous phases (radial chalcedony and crystalline quartz) were probably related to hydrothermal activities. Zhou et al. (2017b) reported homogenization temperatures of fluid inclusions in crystalline quartz at 160–220 °C, which is broadly consistent with a Raman geothermometric study of carbonaceous material in the Doushantuo cap dolostone (Wang et al., 2017). Although it is possible that the siliceous phases may have precipitated from silica-rich fluids derived from burial metamorphism, it is more likely that such fluids were hydrothermal in nature because they do not seem to have pervasively affected the Doushantuo Formation, which has roughly the same burial depth across much of South China. Furthermore, trace element geochemical data (e. g., REE, Ge/Si ratios) indicate that hydrothermal fluids may have contributed to the precipitation of the siliceous phases (Cui et al., 2019). Considering our petrographic observations that isopachous dolomite, fibrous calcite, and speleothems were partially or completely replaced by radial chalcedony and crystalline quartz, we infer that calcareous phases (including isopachous dolomite, fibrous calcite, and speleothems) had precipitated at ambient surface temperatures and were subsequently silicified by hydrothermal siliceous precipitates.

The origin of blocky calcite and blocky dolomite is most controversial. In particular, when and how the block calcite was precipitated is a matter of intense debate. According to published hypotheses, the time of blocky calcite precipitation varies from shortly after cap dolostone deposition to the Cambrian Period, and the alkalinity for blocky calcite precipitation was derived variously from anaerobic oxidation of methane in cold seepages, thermochemical oxidation of thermogenic methane, and hydrothermal fluids (Bristow et al., 2011; Jiang et al., 2003; Wang et al., 2008; Wang et al., 2017). While the origin of blocky calcite remains unresolved, we concur with Zhou et al. (2010) that blocky calcite post-dates isopachous dolomite and fibrous calcite, although its temporal relationship with the silicification is somewhat uncertain. Regardless, we would like to emphasize that the main conclusion of this study (i.e., speleothems in sheet-cavities) is independent of the timing and origins of the siliceous phases and blocky calcite/dolomite, which post-date speleothem precipitation.

7.4.2. A new model

Based on the paragenetic sequence and origins of sheet-cavity cements (Table 2), we propose a new model to account for the field, petrographic, and geochemical data of the Doushantuo cap dolostone. Our model is similar to Zhou et al.'s (2010) model in that the sheet-cavities and the karstification surface atop the cap dolostone are genetically related and were both formed during the post-glacial isostatic rebound, but differ in the time when cementation in sheet-cavities was initiated. In our model, sheet-cavity cementation began during karstification and before the second transgression.

At the termination of the Marinoan glaciation, deglaciation caused a rapid glacioeustatic sea-level rise, global transgression, and global deposition of the basal Ediacaran cap dolostone. Subsequently, post-glacial isostatic rebound occurred at local to regional scales and at a magnitude of several hundred meters (Creveling and Mitrovica, 2014), resulting in a significant sea-level fall in South China and subaerial exposure of the Doushantuo cap dolostone previously deposited in various facies. It is during this episode of subaerial exposure when karstification, sheet-cavity formation, and the early phases of sheet-

cavity cementation occurred in the Doushantuo cap dolostone.

We propose that isopachous dolomite precipitated in the sheet-cavities when the latter were in the phreatic zone where seawater mixed with meteoric water (Fig. 13A–B). The precipitation of isopachous dolomite may have been part of the dissolution and reprecipitation process: the dissolution of cap dolostone may have served as a Mg source for isopachous dolomite precipitation. Thus, isopachous dolomite precipitation was likely influenced by seawater, meteoric water, and cap dolostone dissolution. As such, it is not surprising that isopachous dolomite and the cap dolostone have overlapping $\delta^{13}\text{C}$ – $\delta^{18}\text{O}$ values and REE + Y patterns (Zhao et al., 2018). This scenario is consistent with the interpretation that isopachous dolomite represents primary dolomite cements bearing marine signatures (Wallace et al., 2019), and is also consistent with a LA-ICPMS U–Pb age of 632 ± 17 Ma from the isopachous dolomite (Gan et al., 2021).

We note that the dissolution of the cap dolostone, by itself, is unlikely to produce fluids with Mg/Ca molar ratios greater than one, thus limiting the precipitation of isopachous dolomite. However, the establishment of an epikarst zone may increase $p\text{CO}_2$ and $\text{CO}_2/\text{Ca}^{2+}$ ratio and facilitate dolomitization in the phreatic zone (Moore and Wade, 2013). Further, the formation of calcareous caliche in the epikarst would result in Ca^{2+} removal and Mg^{2+} enrichment, thus elevating the Mg/Ca ratios of the downward percolating fluids that reach the phreatic zone. In addition, seawater incursion in the phreatic zone is another major source of Mg^{2+} supporting isopachous dolomite precipitation. Finally, microorganisms could facilitate Mg^{2+} dehydration, generate alkalinity, consume protons, and mobilize potentially catalyzing ions (i.e., Mn and Zn ions) to accelerate dolomite precipitation (Petrash et al., 2021).

We further propose that the subsequent precipitation of fibrous calcite may have occurred in the vadose zone as local sea-level fall continued, sheet-cavities were raised above the water table, and speleothems began to develop (Fig. 13C–D). Because the sheet-cavities were above the water table, previously precipitated isopachous dolomite experienced little dissolution, as evidenced by the perfect preservation of isopachous dolomite crystal terminations (Fig. 4A–C, 4E, 6A–C). However, changes in fluid chemistry from the phreatic to vadose zone resulted in a mineralogical switch from isopachous dolomite to fibrous calcite precipitation. It is in these speleothems where cavity-dwelling filamentous fungus-like microbes were initially preserved (Gan et al., 2021), and these microfossils provide key evidence for the (re-)establishment of a soil microbial ecosystem after the glaciation.

Both isopachous dolomite and fibrous calcite were then partially or completely silicified by hydrothermal fluids to become the siliceous phases (radial chalcedony and crystalline quartz) (Fig. 13E–F). The silicification probably helped to permanently preserve the microfossils in the siliceous phases. That the microfossils are preferentially preserved in the siliceous phases but not in fibrous calcite indicates that silicification followed shortly after fibrous calcite precipitation and before complete degradation of microbial remains. The silicification probably occurred around 635 Ma (radiometric age from just above the cap dolostone) and certainly before 632 Ma (radiometric age from Member II), because Member II apparently was not affected by this hydrothermal event. This inference is consistent with the occurrence of a chalcedony ring (possible representing a hydrothermal channel) at the karstic surface atop the cap dolostone but truncated by overlying strata at the

Table 2

Inferred paragenetic sequence of sheet-cavity cements in the cap dolostone of the Doushantuo Formation. Paragenetic sequence is inferred from observations of sheet-cavities at the Zhangcunping, Xiaofenghe, Xiangerwan, Jiulongwan, Huajipo, Tianjiayuanzi, Songlin, Beidoushan, Daping, and Wenghui.

	Fluids			Sedimentary environments
	Seawater	Meteoric water	Hydrothermal	
Isopachous dolomite (ID)	—————			Phreatic zone
Fibrous calcite (FC)		—————		Vadose zone
Radial chalcedony (RC)			—————	Hydrothermal
Crystalline quartz (CQ)			—————	Hydrothermal

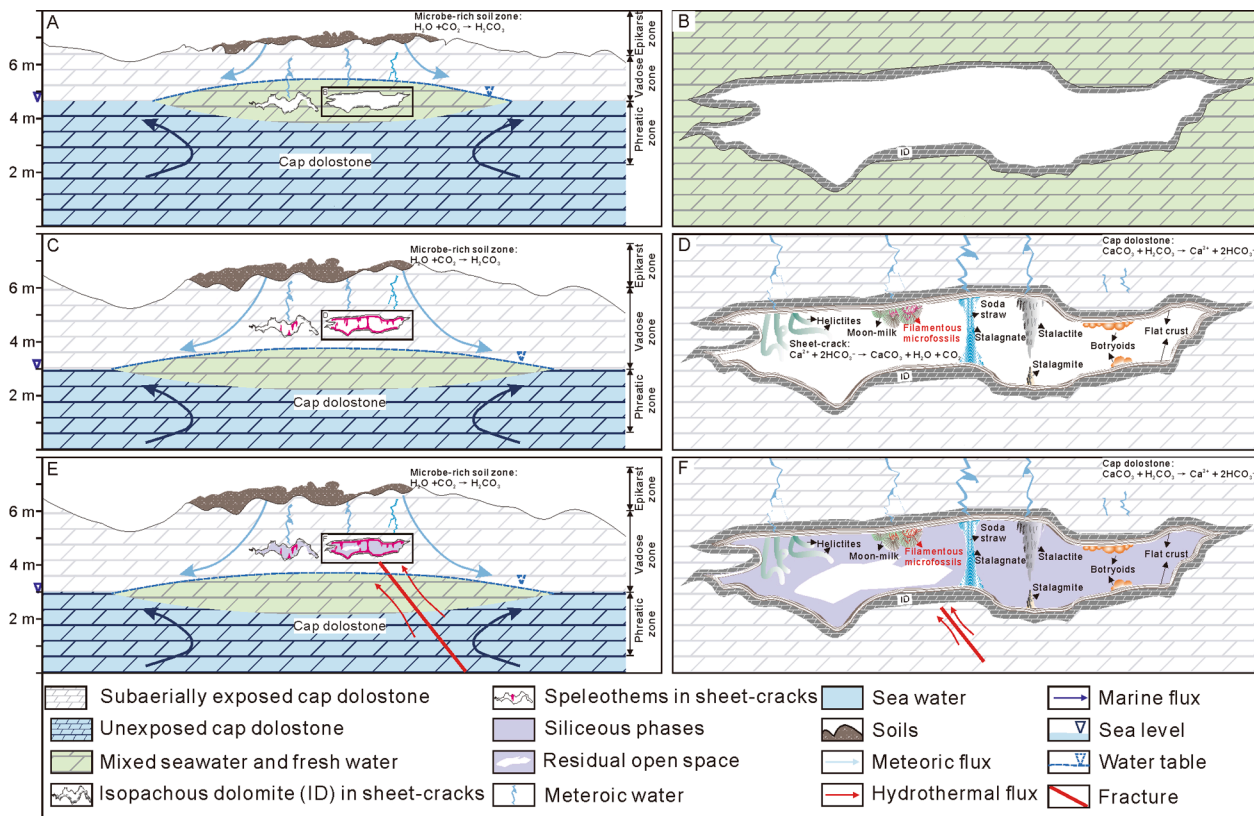


Fig. 13. A conceptual model showing the formation of sheet-cavities, isopachous dolomite, and speleothems in Doushantuo cap dolostone. (A) Post-glacial isostatic rebound exposed cap dolostone above local sea-level. Dissolution, sheet-cavity formation, and isopachous dolomite (ID) precipitation occurred in the phreatic zone. (B) A close-up view of a sheet-cavity in (A), showing ID in sheet-cavity. (C) Local sea-level continued to drop. FC precipitation, speleothems formation, as well as microbial colonization of sheet-cavities occurred when the sheet-cavities were raised to the vadose zone. (D) A close-up view of a sheet-cavity in (C), showing the six types of speleothems described in this paper. (E) Hydrothermal activity event. Siliceous phases precipitated and replaced ID and FC that constitute speleothems. (F) A close-up view of a sheet-cavity in (E), showing the six types of silicified speleothems and the residual space. This model does not address the temporal relationship between silicification and the formation of BC/BD, which remains unresolved. Note that sheet-cavities are millimeters to decimeters in size, and they are not presented to scale. See Fig. 4 for cement abbreviations.

Datang section (Gan et al., 2021, their Fig. S1e), indicating that the siliceous phases were subjected to weathering at the karstic surface.

As discussed above, the exact timing and origin(s) of blocky calcite/dolomite remain uncertain. The blocky calcite/dolomite must post-date the isopachous dolomite and fibrous calcite on the basis of cement stratigraphy, although it is uncertain whether the blocky calcite/dolomite pre- or post-date the silicification event. This uncertainty, however, does not affect the main conclusion of this study: the development of speleothems in the aftermath of the Marinoan snowball Earth, possibly facilitated by an active soil-microbial system.

8. Conclusions and implications

In this study, we investigated the earliest Ediacaran Doushantuo cap dolostone in South China on the basis of integrated field, petrographic, and geochemical data. We documented a widespread karstification surface atop the Doushantuo cap dolostone, demonstrated the role of chemical dissolution in the formation of sheet-cavities within the cap dolostone, and described multiple generations of cements within the sheet-cavities. These cements include isopachous dolomite, isopachous fibrous calcite, isopachous radial chalcidony, crystalline quartz, and blocky calcite/dolomite. We further described six types of paleo-speleothems—including stalactites, stalagmites, helictites, moonmilk, botryoids, and flat crusts—that consist of fibrous calcite and/or radial chalcidony fabrics.

Our study demonstrated a widespread karstification event following the deposition of the Doushantuo cap dolostone. The karstic surface atop

the Doushantuo cap dolostone, sheet-cavities within the cap dolostone, and speleothem precipitation within the sheet-cavities were genetically related to the karstification event. We propose an integrative paragenesis model to account for the temporal and genetic relationship among karstification, sheet-cavity formation, and speleothem precipitation. In this model, post-glacial isostatic rebound caused karstification and augmentation of sheet-cavities, isopachous dolomite was probably precipitated from mixed marine and meteoric waters in the phreatic zone, speleothems with fibrous calcite fabrics were precipitated from meteoric waters in the vadose zone and under the influence of CO₂ degassing, and subsequently, isopachous dolomite and fibrous calcite were partially or completely silicified by siliceous hydrothermal fluids. The relative timing between this silicification event and blocky calcite/dolomite precipitation has not been firmly determined.

The Doushantuo paleo-speleothems have potential implications for soil microbes in the earliest Ediacaran Period and rapid recovery of terrestrial life after the Marinoan snowball Earth. We speculate that soil microbes may have provided organic matter and microbial respiration may have led to elevated CO₂ concentrations in the epikarst zone, which is an important factor driving speleothem formation. This indirect evidence for soil microbes, together with direct evidence of fungus-like filamentous microfossils preserved in Doushantuo speleothems (Gan et al., 2021), offers a strong hint that the terrestrial ecosystem recovered rapidly in the aftermath of the Marinoan snowball Earth glaciation.

The authors declare that they have no known competing financial interests or personal relationships that could have appeared to influence the work reported in this paper.

CRediT authorship contribution statement

Tian Gan: Conceptualization, Writing – original draft, Investigation, Resources, Data curation, Visualization. **Guanghong Zhou:** Conceptualization, Investigation, Writing – original draft. **Taiyi Luo:** Conceptualization, Investigation, Resources, Writing – review & editing, Supervision. **Ke Pang:** Writing – review & editing. **Mingzhong Zhou:** Investigation. **Weijun Luo:** Investigation. **Shijie Wang:** Resources. **Shuhai Xiao:** Conceptualization, Investigation, Resources, Writing – review & editing, Supervision.

Declaration of Competing Interest

The authors declare that they have no known competing financial interests or personal relationships that could have appeared to influence the work reported in this paper.

Acknowledgements

This research was supported by the National Natural Science Foundation of China (U1812402, 41873058, 41802027, 41921002,) and the Science and Technology Foundation of Guizhou Province [JZ(2015)2009, QKH(2018)5778-04]. S.X. was supported by NSF (EAR-2021207). T.G. acknowledges financial support from the China Scholarship Council. K.P. was supported by the Youth Innovation Promotion Association of the Chinese Academy of Sciences (2021307). We thank Chuanming Zhou and Benjamin C. Gill for discussion, and two anonymous reviewers for constructive reviews.

References

- Algeo, T.J., Scheckler, S.E., 1998. Terrestrial-marine teleconnections in the Devonian: Links between the evolution of land plants, weathering processes, and marine anoxic events, Series B: Biological Sciences. *Phil. Trans. R. Soc. Lond. B* 353 (1365), 113–130. <https://doi.org/10.1098/rstb.1998.0195>.
- Álvarez, J.J., Clausen, S., 2010. Morphology and ultrastructure of epilithic versus cryptic, microbial growth in lower Cambrian phosphorites from the Montagne Noire, France. *Geobiology* 8, 89–100. <https://doi.org/10.1111/j.1472-4669.2009.00229.x>.
- An, Z., Jiang, G., Tong, J., Tian, L., Ye, Q., Song, H., Song, H., 2015. Stratigraphic position of the Ediacaran Miaohu biota and its constraints on the age of the upper Doushantuo $\delta^{13}\text{C}$ anomaly in the Yangtze Gorges area, South China. *Precamb. Res.* 271, 243–253. <https://doi.org/10.1016/j.precamres.2015.10.007>.
- Aubrecht, R., Brewer-Carías, C.H., Šmída, B., Audy, M., Kováčik, L., 2008. Anatomy of biologically mediated opal speleothems in the World's largest sandstone cave: Cueva Charles Brewer, Chimantá Plateau, Venezuela. *Sed. Geol.* 203 (3–4), 181–195. <https://doi.org/10.1016/j.sedgeo.2007.10.005>.
- Baker, A., Proctor, C.J., Barnes, W.L., 2002. Stalagmite lamina doublets: a 1000 year proxy record of severe winters in northwest Scotland? *Int. J. Climatol.* 22 (11), 1339–1345. <https://doi.org/10.1002/joc.800>.
- Baker, A., Smart, P.L., Edwards, R.L., Richards, D.A., 1993. Annual growth banding in a cave stalagmite. *Nature* 364 (6437), 518–520. <https://doi.org/10.1038/364518a0>.
- Banks, V., Jones, P., 2012. Hydrogeological significance of secondary terrestrial carbonate deposition in karst environments, in: Gholam, A.K. (Ed.), *Hydrogeology-A Global Perspective*. InTech, Janeza Trdine 9, 51000 Rijeka, Croatia, pp. 43–78. 978-953-51-0048-5.
- Barfod, G.H., Albarède, F., Knoll, A.H., Xiao, S., Télouk, P., Frei, R., Baker, J., 2002. New Lu–Hf and Pb–Pb age constraints on the earliest animal fossils. *Earth Planet. Sci. Lett.* 201 (1), 203–212. [https://doi.org/10.1016/S0012-821X\(02\)00687-8](https://doi.org/10.1016/S0012-821X(02)00687-8).
- Baskar, S., Baskar, R., Routh, J., 2011. Biogenic evidences of moonmilk deposition in the Mawmluh cave, Meghalaya, India. *Geomicrobiol. J.* 28 (3), 252–265. <https://doi.org/10.1080/01490451.2010.494096>.
- Berbee, M.L., Strullu-Derrien, C., Delaux, P.-M., Strother, P.K., Kenrick, P., Selosse, M.-A., Taylor, J.W., 2020. Genomic and fossil windows into the secret lives of the most ancient fungi. *Nat. Rev. Microbiol.* 18 (12), 717–730. <https://doi.org/10.1038/s41579-020-0426-8>.
- Borsato, A., Frisia, S., Jones, B., Van Der Borg, K., 2000. Calcite moonmilk: crystal morphology and environment of formation in caves in the Italian Alps. *J. Sediment. Res.* 70 (5), 1171–1182. <https://doi.org/10.1306/032300701171>.
- Borsato, A., Frisia, S., Miorandi, R., van der Borg, K., Spötl, C., Corradini, F., 2007. Holocene climate and environmental reconstruction from calcareous tufa and moonmilk deposits in Trentino caves. *Acta Geologica* 83, 239–260.
- Brasier, A.T., 2011. Searching for travertines, calcrites and speleothems in deep time: Processes, appearances, predictions and the impact of plants. *Earth Sci. Rev.* 104 (4), 213–239. <https://doi.org/10.1016/j.earscirev.2010.10.007>.
- Bristow, T.F., Bonifacie, M., Derkowski, A., Eiler, J.M., Grotzinger, J.P., 2011. A hydrothermal origin for isotopically anomalous cap dolostone cements from south China. *Nature* 474 (7349), 68–71. <https://doi.org/10.1038/nature10096>.
- Brook, G.A., Rafter, M.A., Railsback, L.B., Sheen, S.-W., Lundberg, J., 1999. A high-resolution proxy record of rainfall and ENSO since AD 1550 from layering in stalagmites from Anjohibe Cave, Madagascar. *The Holocene* 9 (6), 695–705. <https://doi.org/10.1191/095968399677907790>.
- Caddeo, G.A., Railsback, L.B., De Waele, J., Frau, F., 2015. Stable isotope data as constraints on models for the origin of coralloid and massive speleothems: The interplay of substrate, water supply, degassing, and evaporation. *Sed. Geol.* 318, 130–141. <https://doi.org/10.1016/j.sedgeo.2014.12.008>.
- Cañaveras, J.C., Cuezva, S., Sanchez-Moral, S., Lario, J., Laiz, L., Gonzalez, J.M., Saiz-Jimenez, C., 2006. On the origin of fiber calcite crystals in moonmilk deposits. *Naturwissenschaften* 93, 27–32. <https://doi.org/10.1191/095968399677907790>.
- Chafetz, H.S., Butler, J.C., 1980. Petrology of recent caliche pisolites, spherulites, and speleothem deposits from central Texas. *Sedimentology* 27 (5), 497–518. <https://doi.org/10.1111/j.1365-3091.1980.tb01644.x>.
- Chang, Y., Rochon, D.A., Sekimoto, S., Wang, Y., Chovatia, M., Sandor, L., Salamov, A., Grigoriev, I.V., Stajich, J.E., Spatafora, J.W., 2021. Genome-scale phylogenetic analyses confirm *Olpidium* as the closest living zoospore fungus to the non-flagellated, terrestrial fungi. *Sci. Rep.* 11, 3217. <https://doi.org/10.1038/s41598-021-82607-4>.
- Cloud, P., Wright, L.A., Williams, E.G., Diehl, P., Walter, M.R., 1974. Giant stromatolites and associated vertical tubes from the Upper Proterozoic Noonday Dolomite, Death Valley region, eastern California. *Geol. Soc. Am. Bull.* 85, 1869–1882. [https://doi.org/10.1130/0016-7606\(1974\)85%3C1869:GSAAVT%3E2.0.CO;2](https://doi.org/10.1130/0016-7606(1974)85%3C1869:GSAAVT%3E2.0.CO;2).
- Condon, D., Zhu, M., Bowring, S., Wang, W., Yang, A., Jin, Y., 2005. U–Pb Ages from the Neoproterozoic Doushantuo Formation, China. *Science* 308, 95–98. <https://www.science.org/doi/10.1126/science.1107765>.
- Corkeron, MAREE, 2007. 'Cap carbonates' and Neoproterozoic glacial successions from the Kimberley region, north-west Australia. *Sedimentology* 54 (4), 871–903. <https://doi.org/10.1111/j.1365-3091.2007.00864.x>.
- Creveling, J.R., Bergmann, K.D., Grotzinger, J.P., 2016. Cap carbonate platform facies model, Noonday Formation, SE California. *GSA Bulletin* 128 (7–8), 1249–1269. <https://doi.org/10.1130/B31442.1>.
- Creveling, J.R., Mitrova, J.X., 2014. The sea-level fingerprint of a Snowball Earth deglaciation. *Earth Planet. Sci. Lett.* 399, 74–85. <https://doi.org/10.1016/j.epsl.2014.04.029>.
- Cui, Y., Lang, X., Li, F., Huang, K., Ma, H., Li, C., Pei, H., Li, C., Zhou, C., Shen, B., 2019. Germanium/silica ratio and rare earth element composition of silica-filling in sheet cracks of the Doushantuo cap carbonates, South China: Constraining hydrothermal activity during the Marinoan snowball Earth glaciation. *Precamb. Res.* 332, 105407. <https://doi.org/10.1016/j.precamres.2019.105407>.
- Ding, Y.i., Chen, D., Zhou, X., Guo, C., Huang, T., Zhang, G., Brasier, A., 2019. Cavity-filling dolomite speleothems and submarine cements in the Ediacaran Dengying microbialites, South China: Responses to high-frequency sea-level fluctuations in an 'aragonite-dolomite sea'. *Sedimentology* 66 (6), 2511–2537. <https://doi.org/10.1111/sed.12605>.
- Dreybrodt, W., Romanov, D., 2008. Regular stalagmites: The theory behind their shape. *Acta Carsologica* 37, 175–184. <https://doi.org/10.3986/ac.v37i2-3.145>.
- Fairchild, I.J., Baker, A., 2012. Speleothem science: From process to past environments, in: Bradley, R. (Ed.), *The architecture of speleothems*. John Wiley & Sons, The Atrium, Southern Gate, Chichester, West Sussex, PO19 8SQ, UK, pp. 213–222. 1444361074.
- Fairchild, I.J., Frisia, S., Borsato, A., Tooth, A.F., 2006. Speleothems, in: Nash, D.J., McLaren, S.J. (Eds.), *Speleothems in their geomorphic, hydrological and climatological context*. Geochemical Sediments and Landscapes, Blackwell, Oxford, pp. 1–21.
- Freytet, P., Verrecchia, E.P., 2002. Lacustrine and palustrine carbonate petrography: an overview. *J. Paleolimnol.* 27, 221–237. <https://doi.org/10.1023/A:1014263722766>.
- Frisia, S., Borsato, A., Preto, N., McDermott, F., 2003. Late Holocene annual growth in three Alpine stalagmites records the influence of solar activity and the North Atlantic Oscillation on winter climate. *Earth Planet. Sci. Lett.* 216 (3), 411–424. [https://doi.org/10.1016/S0012-821X\(03\)00515-6](https://doi.org/10.1016/S0012-821X(03)00515-6).
- Gammon, P.R., 2012. An organodiagenetic model for Marinoan-age cap carbonates. *Sed. Geol.* 243, 17–32. <https://doi.org/10.1016/j.sedgeo.2011.12.004>.
- Gammon, P.R., McKirdy, D.M., Smith, H.D., 2012. The paragenetic history of a Marinoan cap carbonate. *Sed. Geol.* 243, 1–16. <https://doi.org/10.1016/j.sedgeo.2011.07.004>.
- Gan, T., Luo, T., Pang, K., Zhou, C., Zhou, G., Wan, B., Li, G., Yi, Q., Czaja, A.D., Xiao, S., 2021. Cryptic terrestrial fungus-like fossils of the early Ediacaran Period. *Nat. Commun.* 12, 641. <https://doi.org/10.1038/s41467-021-20975-1>.
- Glover, J.F., 2006. Speleothem deposits in a proterozoic paleokarst, mesoproterozoic distal lakes group, Arctic Canada, Geological Society of America Southeastern Section — 55th Annual Meeting Geological Society of America Abstracts with Programs, Knoxville, Tennessee, USA, p. 36.
- Gribovski, K., Kovács, K., Mónus, P., Bokelmann, G., Konecny, P., Lednická, M., Moseley, G., Spötl, C., Edwards, R.L., Bednárík, M., Brimich, L., Tóth, L., 2017. Estimating the upper limit of prehistoric peak ground acceleration using an in situ, intact and vulnerable stalagmite from Plavecká priepast cave (Detrečkő-zsomboly), Little Carpathians, Slovakia—first results. *J. Seismolog.* 21 (5), 1111–1130. <https://doi.org/10.1007/s10950-017-9655-3>.
- Haas, J., 2004. Characteristics of peritidal facies and evidences for subaerial exposures in Dachstein-type cyclic platform carbonates in the Transdanubian Range, Hungary. *Facies* 50, 263–286. <https://doi.org/10.1007/s10347-004-0021-x>.
- Hoffman, P.F., Abbot, D.S., Ashkenazy, Y., Benn, D.I., Brooks, J.J., Cohen, P.A., Cox, G.M., Creveling, J.R., Donnadiu, Y., Erwin, D.H., Fairchild, I.J., Ferreira, D., Goodman, J.C., Halverson, G.P., Jansen, M.F., Le Hir, G., Love, G.D., Macdonald, F.

- A., Maloof, A.C., Partin, C.A., Ramstein, G., Rose, B.E.J., Rose, C.V., Sadler, P.M., Tziperman, E., Voigt, A., Warren, S.G., 2017. Snowball Earth climate dynamics and Cryogenian geology-geobiology. *Sci. Adv.* 3, e1600983. <https://www.science.org/doi/10.1126/sciadv.1600983>.
- Hoffman, P.F., Macdonald, F.A., 2010. Sheet-crack cements and early regression in Marinoan (635Ma) cap dolostones: Regional benchmarks of vanishing ice-sheets? *Earth Planet. Sci. Lett.* 300 (3-4), 374–384. <https://doi.org/10.1016/j.epsl.2010.10.027>.
- Homann, M., Heubeck, C., Bontognali, T.R.R., Bouvier, A.-S., Baumgartner, L.P., Airo, A., 2016. Evidence for cavity-dwelling microbial life in 3.22 Ga tidal deposits. *Geology* 44 (1), 51–54. <https://doi.org/10.1130/G37272.110.1130/2016012>.
- Homann, M., Sansjofre, P., Van Zuilen, M., Heubeck, C., Gong, J., Killingsworth, B., Foster, L.S., Airo, A., Van Kranendonk, M.J., Ader, M., Lalonde, S.V., 2018. Microbial life and biogeochemical cycling on land 3,220 million years ago. *Nat. Geosci.* 11 (9), 665–671. <https://doi.org/10.1038/s41561-018-0190-9>.
- Hood, A.V.S., Wallace, M.W., 2012. Synsedimentary diagenesis in a Cryogenian reef complex: Ubiquitous marine dolomite precipitation. *Sed. Geol.* 255–256, 56–71. <https://doi.org/10.1016/j.sedgeo.2012.02.004>.
- Hood, A.V.S., Wallace, M.W., Reed, C.P., Hoffmann, K.-H., Freyer, E.E., 2015. Enigmatic carbonates of the Ombombo Subgroup, Otavi Fold Belt, Namibia: A prelude to extreme Cryogenian anoxia? *Sed. Geol.* 324, 12–31. <https://doi.org/10.1016/j.sedgeo.2015.04.007>.
- Huff, L.C., 1940. Artificial helictites and gypsum flowers. *J. Geol.* 48 (6), 641–659. <https://doi.org/10.1086/624919>.
- Jiang, G., Kennedy, M.J., Christie-Blick, N., Wu, H., Zhang, S., 2006. Stratigraphy, sedimentary structures, and textures of the late Neoproterozoic Doushantuo cap carbonate in South China. *J. Sediment. Res.* 76 (7), 978–995. <https://doi.org/10.2110/jsr.2006.086>.
- Jiang, G., Kennedy, M.J., Christie-Blick, N., 2003. Stable isotopic evidence for methane seeps in Neoproterozoic postglacial cap carbonates. *Nature* 426 (6968), 822–826. <https://doi.org/10.1038/nature02201>.
- Jiang, G., Shi, X., Zhang, S., Wang, Y., Xiao, S., 2011. Stratigraphy and paleogeography of the Ediacaran Doushantuo Formation (ca. 635–551 Ma) in South China. *Gondwana Res.* 19 (4), 831–849. <https://doi.org/10.1016/j.jgr.2011.01.006>.
- Jiang, G., Zhang, S., Shi, X., Wang, X.J.S.I.C.S.D.E.S., 2008. Chemocline instability and isotope variations of the Ediacaran Doushantuo basin in South China. *Science in China Series D: Earth Sciences* 51, 1560–1569. <https://doi.org/10.1007/s11430-008-0116-2>.
- Jones, B., 2011. Stalactite growth mediated by biofilms: Example from Nani cave, Cayman Brac, British West Indies. *J. Sediment. Res.* 81 (4), 322–338. <https://doi.org/10.2110/jsr.2011.28>.
- Kaufmann, G., 2003. Stalagmite growth and palaeo-climate: the numerical perspective. *Earth Planet. Sci. Lett.* 214 (1–2), 251–266. [https://doi.org/10.1016/S0012-821X\(03\)00369-8](https://doi.org/10.1016/S0012-821X(03)00369-8).
- Kennedy, M., Droser, M., Mayer, L.M., Pevear, D., Mrofka, D., 2006. Late Precambrian oxygenation: inception of the clay mineral factory. *Science* 311, 1446–1449. <https://www.science.org/doi/full/10.1126/science.1118929>.
- Kump, L.R., 2014. Hypothesized link between Neoproterozoic greening of the land surface and the establishment of an oxygen-rich atmosphere. *Proc. Natl. Acad. Sci.* 111 (39), 14062–14065. <https://doi.org/10.1073/pnas.1321496111>.
- Lacelle, D., Lauriol, B., Clark, I.D., 2004. Seasonal isotopic imprint in moonmilk from Caverne de l'Ours (Quebec, Canada): implications for climatic reconstruction. *Can. J. Earth Sci.* 41 (12), 1411–1423. <https://doi.org/10.1139/e04-080>.
- Liu, P., Moczydlowska, M., 2019. Ediacaran microfossils from the Doushantuo Formation chert nodules in the Yangtze Gorges Area, South China, and new biozones, Fossils and Strata. John Wiley & Sons, Chichester, p. 173.
- Liu, P., Xiao, S., Yin, C., Chen, S., Zhou, C., Li, M., 2014. Ediacaran acanthomorphic acritarchs and other microfossils from chert nodules of the upper Doushantuo Formation in the Yangtze Gorges area, South China. *J. Paleontol.* 88 (S72), 1–139. <https://doi.org/10.1666/13-009>.
- Liu, P., Yin, C., Gao, L., Tang, F., Chen, S., 2009. New material of microfossils from the Ediacaran Doushantuo Formation in the Zhangcunping area, Yichang, Hubei Province and its zircon SHRIMP U-Pb age. *Chin. Sci. Bull.* 54 (6), 1058–1064. <https://doi.org/10.1007/s11434-008-0589-6>.
- Lu, M., Zhu, M., Zhao, F., 2012. Revisiting the Tianjiayuanzi section - the stratotype section of the Ediacaran Doushantuo Formation, Yangtze Gorges, South China. *Bull. Geosci.* 87, 183–194. <https://doi.org/10.3140/bull.geosci.1227>.
- Lutzoni, F., Nowak, M.D., Alfaro, M.E., Reeb, V., Miadlikowska, J., Krug, M., Arnold, A. E., Lewis, L.A., Swofford, D.L., Hibbett, D., Hilu, K., James, T.Y., Quandt, D., Magallón, S., 2018. Contemporaneous radiations of fungi and plants linked to symbiosis. *Nat. Commun.* 9, 5451. <https://doi.org/10.1038/s41467-018-07849-9>.
- McFadden, K.A., Huang, J., Chu, X., Jiang, G., Kaufman, A.J., Zhou, C., Yuan, X., Xiao, S., 2008. Pulsed oxidation and biological evolution in the Ediacaran Doushantuo Formation. *Proc. Natl. Acad. Sci.* 105 (9), 3197–3202. <https://doi.org/10.1073/pnas.0708336105>.
- Moore, C.H., Wade, W.J., 2013. Chapter 8 - Meteoric Diagenetic Environment. In: Moore, C.H., Wade, W.J. (Eds.), *Developments in Sedimentology*. Elsevier, pp. 165–206. <https://doi.org/10.1016/B978-0-444-53831-4.00008-2>.
- Noffke, N., Eriksson, K.A., Hazen, R.M., Simpson, E.L., 2006. A new window into Early Archean life: Microbial mats in Earth's oldest siliciclastic tidal deposits (3.2 Ga Moodies Group, South Africa). *Geology* 34, 253–256. <https://doi.org/10.1130/G22246.1>.
- Onuk, P., Dietzel, M., Hauenberger, C.A., 2014. Formation of helictite in the cave Dragon Belly (Sardinia, Italy)—Microstructure and incorporation of Mg, Sr, and Ba. *Geochemistry* 74 (3), 443–452. <https://doi.org/10.1016/j.chemer.2014.04.003>.
- Ouyang, Q., Zhou, C., Xiao, S., Chen, Z., Shao, Y., 2019. Acanthomorphic acritarchs from the Ediacaran Doushantuo Formation at Zhangcunping in South China, with implications for the evolution of early Ediacaran eukaryotes. *Precamb. Res.* 320, 171–192. <https://doi.org/10.1016/j.precamres.2018.10.012>.
- Petrash, D.A., Bialik, O.M., Staudigel, P.T., Konhauser, K.O., Budd, D.A., 2021. Biogeochemical reappraisal of the freshwater-seawater mixing-zone diagenetic model. *Sedimentology* 68, 1797–1830. <https://doi.org/10.1111/sed.12849>.
- Prave, A.R., 2002. Life on land in the Proterozoic: Evidence from the Torridonian rocks of northwest Scotland. *Geology* 30, 811–814. [https://doi.org/10.1130/0091-7613\(2002\)030%3C0811:LOLITP%3E2.0.CO;2](https://doi.org/10.1130/0091-7613(2002)030%3C0811:LOLITP%3E2.0.CO;2).
- Railsback, L.B., Liang, F., Brook, G.A., Voarintsoa, N.R.G., Sletten, H.R., Marais, E., Hardt, B., Cheng, H., Edwards, R.L., 2018. The timing, two-pulsed nature, and variable climatic expression of the 4.2 ka event: A review and new high-resolution stalagmite data from Namibia. *Quat. Sci. Rev.* 186, 78–90. <https://doi.org/10.1016/j.quascirev.2018.02.015>.
- Rasmussen, B., Blake, T.S., Fletcher, I.R., Kilburn, M.R., 2009. Evidence for microbial life in synsedimentary cavities from 2.75 Ga terrestrial environments. *Geology* 37 (5), 423–426. <https://doi.org/10.1130/G25300A.110.1130/2009105>.
- Retallack, G.J., 2003. Soils and global change in the carbon cycle over geological Time. In: Holland, H.D., Turekian, K.K. (Eds.), *Treatise on Geochemistry*. Pergamon, Oxford, pp. 1–28. <https://doi.org/10.1016/B0-08-043751-6/05087-8>.
- Retallack, G.J., 2021. Paleosols and weathering leading up to Snowball Earth in central Australia. *Aust. J. Earth Sci.* 68 (8), 1122–1148. <https://doi.org/10.1080/08120099.2021.1906747>.
- Retallack, G.J., Broz, A.P., Lai, L.-H., Gardner, K., 2021. Neoproterozoic marine chemostratigraphy, or eustatic sea level change? *Palaeogeography, Palaeoclimatology, Palaeoecology* 562, 110155. <https://doi.org/10.1016/j.palaeo.2020.110155>.
- Retallack, G.J., Gose, B.N., Osterhout, J.T., 2015. Periglacial paleosols and Cryogenian paleoclimate near Adelaide, South Australia. *Precamb. Res.* 263, 1–18. <https://doi.org/10.1016/j.precamres.2015.03.002>.
- Romero, G.R., Sanchez, E.A.M., Soares, J.L., Nogueira, A.C.R., Fairchild, T.R., 2020. Waxing and waning of microbial laminites in the aftermath of the Marinoan glaciation at the margin of the Amazon Craton (Brazil). *Precamb. Res.* 348, 105856. <https://doi.org/10.1016/j.precamres.2020.105856>.
- Shields, G.A., Deynoux, M., Strauss, H., Paquet, H., Nahon, D., 2007. Barite-bearing cap dolostones of the Taoudéni Basin, northwest Africa: Sedimentary and isotopic evidence for methane seepage after a Neoproterozoic glaciation. *Precamb. Res.* 153 (3–4), 209–235. <https://doi.org/10.1016/j.precamres.2006.11.011>.
- Skotnicki, S.J., Knauth, L.P., 2007. The middle Proterozoic Mescal paleokarst, central Arizona, U.S.A.: Karst development, silicification, and cave deposits. *J. Sediment. Res.* 77 (12), 1046–1062. <https://doi.org/10.2110/jsr.2007.094>.
- Spatafora, J.W., Chang, Y., Benny, G.L., Lazarus, K., Smith, M.E., Berbee, M.L., Bonito, G., Corradi, N., Grigoriev, I., Gryganskyi, A., James, T.Y., O'Donnell, K., Roberson, R.W., Taylor, T.N., Uehling, J., Vilgaly, R., White, M.M., Stajich, J.E., 2016. A phyllum-level phylogenetic classification of zygomycete fungi based on genome-scale data. *Mycologia* 108 (5), 1028–1046. <https://doi.org/10.3852/16-042>.
- Tan, L., Yi, L., Cai, Y., Shen, C.-C., Cheng, H., An, Z., 2013. Quantitative temperature reconstruction based on growth rate of annually-layered stalagmite: a case study from central China. *Quat. Sci. Rev.* 72, 137–145. <https://doi.org/10.1016/j.quascirev.2013.04.022>.
- Tan, M., Baker, A., Genty, D., Smith, C., Esper, J., Cai, B., 2006. Applications of stalagmite laminae to paleoclimate reconstructions: Comparison with dendrochronology/climatology. *Quat. Sci. Rev.* 25 (17–18), 2103–2117. <https://doi.org/10.1016/j.quascirev.2006.01.034>.
- Thomazo, C., Couradeau, E., Garcia-Pichel, F., 2018. Possible nitrogen fertilization of the early Earth Ocean by microbial continental ecosystems. *Nat. Commun.* 9, 2530. <https://doi.org/10.1038/s41467-018-04995-y>.
- van der Heijden, M.G.A., Bardgett, R.D., van Straalen, N.M., 2008. The unseen majority: soil microbes as drivers of plant diversity and productivity in terrestrial ecosystems. *Ecol. Lett.* 11 (3), 296–310. <https://doi.org/10.1111/j.1461-0248.2007.01139.x>.
- van Maldegem, L.M., Sansjofre, P., Weijers, J.W.H., Wolkenstein, K., Strother, P.K., Wörmer, L., Heftner, J., Nettersheim, B.J., Hoshino, Y., Schouten, S., Sinninghe Damsté, J.S., Nath, N., Griesinger, C., Kuznetsov, N.B., Elie, M., Elvert, M., Tegelaar, E., Gleixner, G., Hallmann, C., 2019. Bisnorgammacerane traces predatory pressure and the persistent rise of algal ecosystems after Snowball Earth. *Nat. Commun.* 10, 476. <https://doi.org/10.1038/s41467-019-08306-x>.
- Verheyden, S., Keppens, E., Fairchild, I.J., McDermott, F., Weis, D., 2000. Mg, Sr and Sr isotope geochemistry of a Belgian Holocene speleothem: implications for paleoclimate reconstructions. *Chem. Geol.* 169 (1–2), 131–144. [https://doi.org/10.1016/S0009-2541\(00\)00299-0](https://doi.org/10.1016/S0009-2541(00)00299-0).
- Wallace, M.W., Hood, A.V.S., Fayle, J., Hordern, E.S., O'Hare, T.F., 2019. Neoproterozoic marine dolomite hardgrounds and their relationship to cap dolomites. *Precamb. Res.* 328, 269–286. <https://doi.org/10.1016/j.precamres.2019.04.026>.
- Wang, J., Jiang, G., Xiao, S., Li, Q., Wei, Q., 2008. Carbon isotope evidence for widespread methane seeps in the ca. 635 Ma Doushantuo cap carbonate in south China. *Geology* 36 (5), 347. <https://doi.org/10.1130/G24513A.1>.
- Wang, Y.e., Wang, Y., Du, W., Wang, X., 2016. New data of macrofossils in the Ediacaran Wenghui biota from Guizhou, South China. *Acta Geologica Sinica (English Edition)* 90 (5), 1611–1628. <https://doi.org/10.1111/1755-6724.12805>.
- Wang, Z., Wang, J., Kouketsu, Y., Bodnar, R.J., Gill, B.C., Xiao, S., 2017. Raman geothermometry of carbonaceous material in the basal Ediacaran Doushantuo cap dolostone: the thermal history of extremely negative $\delta^{13}\text{C}$ signatures in the aftermath of the terminal Cryogenian snowball Earth glaciation. *Precamb. Res.* 298, 174–186. <https://doi.org/10.1111/1755-6724.12805>.

- Wei, H., Wang, X., Shi, X., Jiang, G., Tang, D., Wang, L., An, Z., 2019. Iodine content of the carbonates from the Doushantuo Formation and shallow ocean redox change on the Ediacaran Yangtze Platform, South China. *Precamb. Res.* 322, 160–169. <https://doi.org/10.1016/j.precamres.2019.01.007>.
- Wellman, C.H., Strother, P.K., Smith, A., 2015. The terrestrial biota prior to the origin of land plants (embryophytes): a review of the evidence. *Palaeontology* 58 (4), 601–627. <https://doi.org/10.1111/pala.12172>.
- White, W.B., 2005. Speleothems. In: White, W.B., Culver, D.C., Pipan, T. (Eds.), *Encyclopedia of Caves*, Third ed. Academic Press, SPI Global, India, pp. 1006–1017. <https://doi.org/10.1016/B978-0-12-814124-3.00001-7>.
- Xiao, S., Bykova, N., Kovalick, A., Gill, B.C., 2017. Stable carbon isotopes of sedimentary kerogens and carbonaceous microfossils from the Ediacaran Miaohu Member in South China: Implications for stratigraphic correlation and sources of sedimentary organic carbon. *Precamb. Res.* 302, 171–179. <https://doi.org/10.1016/j.precamres.2017.10.006>.
- Xiao, S., McFadden, K.A., Peek, S., Kaufman, A.J., Zhou, C., Jiang, G., Hu, J., 2012. Integrated chemostratigraphy of the Doushantuo Formation at the northern Xiaofenghe section (Yangtze Gorges, South China) and its implication for Ediacaran stratigraphic correlation and ocean redox models. *Precamb. Res.* 192, 125–141. <https://doi.org/10.1016/j.precamres.2011.10.021>.
- Xiao, S., Muscente, A., Chen, L., Zhou, C., Schiffbauer, J.D., Wood, A.D., Polys, N.F., Yuan, X., 2014a. The Weng'an biota and the Ediacaran radiation of multicellular eukaryotes. *Natl. Sci. Rev.* 1, 498–520. <https://doi.org/10.1093/nsr/nwu061>.
- Xiao, S., Yuan, X., Steiner, M., Knoll, A.H., 2002. Macroscopic carbonaceous compressions in a terminal Proterozoic shale: a systematic reassessment of the Miaohu biota, South China. *J. Paleontol.* 76, 347–376. [https://doi.org/10.1666/0022-3360\(2002\)076%3C0347:MCCLAT%3E2.0.CO;2](https://doi.org/10.1666/0022-3360(2002)076%3C0347:MCCLAT%3E2.0.CO;2).
- Xiao, S., Zhou, C., Liu, P., Wang, D., Yuan, X., 2014b. Phosphatized acanthomorphic acritarchs and related microfossils from the Ediacaran Doushantuo formation at Weng'an (South China) and their implications for biostratigraphic correlation. *J. Paleontol.* 88 (1), 1–67. <https://doi.org/10.1666/12-157R>.
- Yang, C., Rooney, A.D., Condon, D.J., Li, X., Grazhdankin, D.V., Bowyer, F.T., Hu, C., Macdonald, F.A., Zhu, M., 2021. The tempo of Ediacaran evolution. *Science Advances* 7, eabi9643. <https://www.science.org/doi/full/10.1126/sciadv.abi9643>.
- Yuan, X., Xiao, S., Taylor, T.N., 2005. Lichen-like symbiosis 600 million years ago. *Science* 308, 1017–1020. <https://www.science.org/doi/full/10.1126/science.1111347>.
- Zhang, Y., Du, Y., Liu, J., Wang, Z., Deng, C., 2020. Phosphogenesis of phosphorite from the Sinian Doushantuo Formation in Guizhou Province and its coupling relation with the Neoproterozoic Oxygenation Event. *J. Palaeogeography (Chinese edition)* 22, 893–912.
- Zhao, Y., Zhao, M., Li, S., 2018. Evidences of hydrothermal fluids recorded in microfacies of the Ediacaran cap dolostone: Geochemical implications in South China. *Precamb. Res.* 306, 1–21. <https://doi.org/10.1016/j.precamres.2017.12.028>.
- Zhou, C., Bao, H., Peng, Y., Yuan, X., 2010. Timing the deposition of ^{17}O -depleted barite at the aftermath of Nantuo glacial meltdown in South China. *Geology* 38 (10), 903–906. <https://doi.org/10.1130/G31224.1>.
- Zhou, C., Lang, X., Huyskens, M.H., Yin, Q., Xiao, S., 2019. Calibrating the terminations of Cryogenian global glaciations. *Geology* 47, 251–254. <https://doi.org/10.1130/G45719.1>.
- Zhou, C., Li, X., Xiao, S., Lan, Z., Ouyang, Q., Guan, C., Chen, Z., 2017a. A new SIMS zircon U-Pb date from the Ediacaran Doushantuo Formation: age constraint on the Weng'an biota. *Geol. Mag.* 154 (6), 1193–1201. <https://doi.org/10.1017/S0016756816001175>.
- Zhou, G., Luo, T., Zhou, M., Xing, L., Gan, T., 2017b. A ubiquitous hydrothermal episode recorded in the sheet-crack cements of a Marinoan cap dolostone of South China: Implication for the origin of the extremely ^{13}C -depleted calcite cement. *J. Asian Earth Sci.* 134, 63–71. <https://doi.org/10.1016/j.jseas.2016.11.007>.
- Zhu, M., Gehling, J.G., Xiao, S., Zhao, Y., Droser, M.L., 2008. Eight-armed Ediacara fossil preserved in contrasting taphonomic windows from China and Australia. *Geology* 36 (11), 867. <https://doi.org/10.1130/G25203A.1>.